UNIVERSITY OF OKLAHOMA

GRADUATE COLLEGE

THE EFFECTS OF URBAN GEOMETRY ON POINT SOURCE SCALAR PLUME STATISTICS: A LARGE EDDY SIMULATION STUDY

A THESIS

SUBMITTED TO THE GRADUATE FACULTY

in partial fulfillment of the requirements for the

Degree of

MASTER OF SCIENCE IN METEOROLOGY

By

Robert Van Kleeck
Norman, Oklahoma
2020

THE EFFECTS OF URBAN GEOMETRY ON POINT SOURCE SCALAR PLUME STATISTICS: A LARGE EDDY SIMULATION STUDY

A THESIS APPROVED FOR THE
SCHOOL OF METEOROLOGY

BY THE COMMITTEE CONSISTING OF

Dr. Scott Salesky, Chair

Dr. Petra Klein

Dr. Brad Illston

Acknowledgments

This work would not have been possible without the unwavering support of my advisor, Dr. Scott Salesky. Without his guiding and timely advice throughout this multi-year process, this caliber of work would seem distant. The support of my other committee members was invaluable; Dr. Klein helped to solidify my results with poised and thoughtful criticism. Dr. Illston, I owe much of my success in academia to my time with you in REU - I cannot thank you enough for that experience.

I must also thank my partner Alexandra for never failing to reassure my strengths and cast doubt on harsh self-judgement. Your emotional pillar and its personal impact are nothing short of spectacular.

And finally, to my family and friends near or far. Mom and Dad - you've stood by my side in my quest for more, always there with practical and encouraging advice. Will would be so proud of all you've done for us, I can vouch for that. Ben and Elizabeth - hold steady to what interests you, let it define yourself, and do not let *anyone* tell you otherwise. OU, New York, and Lyndon friends (oh YES), I owe my work ethic and energy to our time together - I will cherish that forever.

Table of Contents

Acknowledgments **iv**

List of Tables **vi**

List of Figures **vii**

Abstract **xiii**

1 Introduction **1**
1.1 Overview 1
1.2 Atmospheric Boundary Layer 2
1.2.1 Urban Boundary Layer 4
1.3 Gaussian Dispersion Models 6
1.4 Large Eddy Simulations 9
1.4.1 Urban LES Studies 11
1.5 Research Questions 15

2 Methods **17**
2.1 Overview of Large Eddy Simulation 17
2.1.1 Parameter Space 19
2.2 Plume Moments 24
2.3 Instantaneous Towers 26

3 Results **32**
3.1 Flow Characteristics 32
3.2 Scalar Plume Structure 35
3.3 Exposure Statistics 39

4 Conclusions **49**

Reference List **50**

List of Tables

2.1 Overview of computational parameters used for the plume moment simulations. dt is the computational timestep, Q_{src} is the point source strength is number of particles per second, $\{N_x \times N_y \times N_z\}$ is the numerical discretization, $\{L_x \times L_y \times L_z\}$ is the domain size, and $\Delta x, \Delta y, \Delta z$ is the approximate grid spacing in each direction. 23

2.2 Overview of source locations for each configuration. Coordinates are given in meters. 24

List of Figures

1.1 Diurnal variable of the ABL as portrayed by Stull (1988). Time is on the x axis and height is on the y axis. 3

1.2 Assorted regions of the UBL - adapted from (Fernando 2010). Conventional logarithmic profiles using d and z_0 (displacement and roughness heights, respectively) and in-canopy profiles proposed by (Cionco 1965) are shown. 5

1.3 Schematic of a two dimensional plume from Stockie (2012). The dominate wind flow is in the x direction, leading to lateral and vertical spread of the plume denoted by σ_y and σ_z respectively. 8

1.4 Adapted figure from Giometto et al. (2016). Separate along-canyon and cross-canyon simulations are shown on the left and right respectively. Double-averaged and temporally averaged vertical velocity components from the LES are shown, with the data coming from the tower location in the domain. Tower data is given by the red error bars. Normalized height is on the y axis and the mean vertical velocity is on the x axis. 12

1.5 Adapted figure from Tseng et al. (2006). Timeseries (a) and Probability Density Function (b) of normalized concentration at a downstream location from two point-sources. Various heights at this location are denoted by line type. Concentration on both plots is normalized by $C_0 = u^*/Q$ where u^* is the friction velocity and Q is the source strength. 13

1.6 LES domain used by Philips et al. (2013). Various source locations are shown, and were placed near the tallest and shortest mode of cuboid (A and B, respectively). 14

1.7 Adapted figure from Philips et al. (2013). Source locations are denoted by the black and blue lines, which correspond to locations A and B in Figure 1.6 respectively. Normalized distance downstream of the source is on the x axis, and source height is given by line type. Plume width (equivalent to second plume moment) for the horizontal and vertical are the top and bottom panels respectively, with a linear and log-log scale for each on the left and right panels respectively. 16

2.1 Comparison of aligned and staggered urban geometry, respectively. Source locations are shown for reference. 19

2.2 Various turbulence statistics compared at different numerical discretizations. Panels a), b), and c) show the horizontally averaged resolved velocity variance for the streamwise, spanwise, and vertical velocity components, respectively. These variances are all normalized by the friction velocity squared. Panel d) shows the combination of the resolved stresses and contribution from the SGS. Panel e) shows the horizontally averaged turbulent kinetic energy (TKE) of each flow. Panel f) shows the normalized temporal and spatially averaged streamwise velocity. Vertical distance is normalized by building height H. The 192^2 simulation is highlighted in black to better highlight the discretization of choice. The top of the buildings is marked by the dotted black line at $z/H = 1$ 21

2.3 Cross-sections of time-averaged concentration for a well-developed plume. The left panel shows a cross-section with height fixed at source height; the right panel shows a cross-section with lateral distance fixed at y_{src}. Appropriate horizontal and vertical moments are shown for the horizontal and vertical slices respectively. Time averaged concentration is show on a log-scale,and normalized by the friction velocity u_*, source height H, and source strength q_{src}. 25

2.4 Depiction of tower locations on the medium density, aligned geometry setup. The solid line is the lateral plume centerline from the moment calculations, and the dotted lines represent the $\pm 2\sigma_y$ of the same plume. Pure data driven tower locations are shown by the blue circles; the moved tower locations shown in with the red crosses. The tower in the top right is the "northeast" tower, followed by (counterclockwise from that tower) north, northwest, west, center, and east towers. The three towers at the bottom of the domain along $-2\sigma_y$ are not used. 27

2.5 Example timeseries of instantaneous concentration from an ensemble member. Normalized concentration is shown on the y axis, while time is on the x axis. $\pm 1\sigma_c$ is denoted by the dotted black line, and is used as the threshold for exposure times. Time above the threshold is shaded, and would contribute to a distribution of exposure times for each individual event. The sampled height is at 1.75 meters above the street $N_z = 9$ or $z/H = 0.175$ . . 29

2.6 Example timeseries of instantaneous concentration from a two ensemble members. Normalized scalar concentration is shown on the y axis, and time is on the x axis. The sampled height is at 1.75 meters above the street $N_z = 9$ or $z/H = 0.175$. The concentration statistics are only taken from the sample period from 95 seconds to 175 seconds. 31

3.1 2D cross-sections of time-averaged normalized velocities for the two idealized urban geometries at constant height. Each cross section is at $z/H = 0.5$. The top panels are for the aligned geometry, and the bottom panels are for the staggered geometry. Panels a) and d) show time-averaged streamwise velocity, panels b) and e) show time-averaged spanwise velocity, and panels c) and f) show time-averaged vertical velocity. All velocities are normalized by the friction velocity u^*. 33

3.2 Vertical profile of normalized, double averaged (DA) streamwise velocity. Normalized height is on the y axis, and the top of the cuboids is marked by $z/H = 1$. 34

3.3 Comparison of momentum statistics between the aligned and staggered idealized canopies.Panels a), b), and c) show the horizontally averaged resolved velocity variance for the streamwise, spanwise, and vertical velocity components, respectively. These variances are all normalized by the friction velocity squared. Panel d) shows the combination of the resolved stresses and contribution from the SGS. Panel e) shows the horizontally averaged turbulent kinetic energy (TKE) of each flow. Vertical distance is normalized by building height H. The max shear region at $z/H = 1$ is marked for convenience. 36

3.4 2D cross-sections of time-averaged normalized concentration for the three idealized canopy setups. Contours are given in $\frac{\overline{C}u^*}{HQ_{src}}$ on a log scale from 10^{-8} to 10^{-2}. Panels a), c), and e) are XY cross-sections with z at z_{src} for the aligned, aligned in-street, and staggered canopy setups respectively. Panels b), d), and f) are XZ cross-sections with y at y_{src} for the aligned, aligned in-street, and staggered canopy setups respectively. The first and second plume moments are overlaid for each case. 37

3.5 Plume moments for all nine of the simulations. Line type denotes source height, line color denotes geometry/placement. Each row represents a specific moment; Panels a) and b) refer to mean centerline, c) and d) the standard deviation (spread), e) and f) the skewness, and g) and h) the kurtosis. The columns denote the dimension of the moment; the left column refers to horizontal moments, and the right column refers to vertical moments. Downstream distances and moment values are normalized by the building height H. 40

3.6 Maximum time-averaged concentration downstream from the source on a log-scale vs normalized distance from the source. 41
3.7 JPDFs for filtered instantaneous normalized streamwise and vertical velocity components, along with normalized scalar concentration values. Tower data is from the $\mu_z = 1.5H$ centerline tower at height $z/H \approx 1$. Contours are on a log scale from 0.001 to 0.4 42
3.8 JPDFs for filtered instantaneous normalized streamwise and vertical velocity components, along with normalized scalar concentration values. Tower data is from the $\mu_z = 1.5H$ centerline tower at height $z/H = 0.15$. Contours are on a log scale from 0.001 to 0.4 43
3.9 JPDFs for filtered instantaneous normalized streamwise and vertical velocity components, along with normalized scalar concentration values. Tower data is from the $\mu_z = 1.5H$, $2\sigma_y$ (north) tower at height $z/H = 1$. Contours are on a log scale from 0.001 to 0.4 43
3.10 Probability density functions for each of the six towers in the medium, aligned, source-behind-street ensembles. Eight ensemble members are included here, and the height for each of the towers is 1.75 m above the bottom of the street canyon. Line type denotes centerline vs. $2\sigma_y$ towers. A $+1\sigma_c$ threshold is used. 44
3.11 PDFs of raw (left) and normalized (right) concentration at each of the six tower locations. Height is 1.75 meters above the bottom of the street canyons. Dashed lines denote the northern $(+2\sigma_y)$ towers. The mean line is marked by a dashed grey line at $c'/\sigma_c = 0$ on the normalized plot. 46

3.12 Collage of tower concentrations at the same height from one ensemble member. Panels a), c), and e) are for towers along the spanwise plume centerline (west, center, and east towers, respectively). Panels b), d), and f) are for towers along the $+2\sigma_y$ plume moment (northwest, north, and northeast, respectively). Concentration is on the y axis for each plot, with the entire tower sample period on the x axis. Separate y scales on the centerline and north towers are given for the sake of showing the contrasting behavior more effectively. 47

3.13 Collage of normalized tower concentrations at the same height from one ensemble member. Panels a), c), and e) are for towers along the spanwise plume centerline (west, center, and east towers, respectively). Panels b), d), and f) are for towers along the $+2\sigma_y$ plume moment (northwest, north, and northeast, respectively). Normalized concentration is on the y axis for each plot, with the entire tower sample period on the x axis. The mean concentration for each individual ensemble is marked by a dotted black line. 48

Abstract

Urban population currently forms the largest percentage of total human population in recorded history. The United Nations reported that 54% of people lived in urban environments in 2015, which is slated to increase to 68% by 2050. Preparing for this massive shift requires anticipating possible health hazards to a metropolitan population, and urban meteorology forms a distinct part of this anticipation. Understanding the impact of large urban cores and central business districts (CBDs) on air quality and urban dispersion will help city planners work towards neighborhoods with effective and safe removal of potentially harmful pollutants, like PM2.5. This requires a framework to understand how pollutants are dispersed in an urban canopy.

Advances in Large Eddy Simulations (LES) in recent years facilitate studying this dispersion in more detail. Entire CBDs can be resolved within the domain of the LES, making it very attractive for urban meteorology. This study aims to utilize LES to quantify scalar plumes in an idealized urban canopy at atmospheric Reynolds numbers. A suite of LES was run over idealized urban geometry (cuboids), featuring both staggered and aligned geometry and identical plan and frontal area fractions. Non-Gaussian plume behavior was found in the near source region ($x/H < 12$), although the urban geometry was found to lose its influence on the plume as distance downstream from the source increased. Evidence of street channeling on the plume moments was also found, namely in the form of excess positive kurtosis (K) values (leptokurtic) with an in-street scalar source. In addition to the plume statistics, the behavior of instantaneous scalar concentration at a point (relevant for an individual's exposure to pollutants) is of great interest. Probability distribution functions (PDFs) of scalar concentration, joint PDFs of concentration and velocity fluctuations, and PDFs of time periods that concentration exceeds a set threshold were created to characterize the local behavior of scalar concentration and how it differs from average plume behavior. Non-Gaussian, exponential PDFs were found away from the plume mean centerline, yielding evidence of intermittent instantaneous scalar behavior on the edges of the

plume. These findings emphasize the importance of exercising caution in the near source region when using operational Gaussian dispersion models.

Chapter 1

Introduction

1.1 Overview

With nearly two thirds of the world population slated to live in urban environments by 2050 (GHO 2015; UNDESA 2018), understanding pollutant dispersion and exposure in urban environments has never been more crucial. The complexities of atmospheric flow in urban environments makes modeling this extraordinarily challenging, from both a computational and parameterization standpoint (Britter and Hanna 2003). Many methods have been developed to model urban dispersion, but some of the more popular methods are Gaussian dispersion models; they enjoy widespread use in the atmospheric dispersion community, mainly due to their computational efficiency and relative accuracy at large scales. But for more complex terrain and locations near the source, evidence for non-Gaussian plume statistics is clear (Belcher et al. 2015). The advancement of large eddy simulations (LES) in recent years facilitates studying these non-Gaussian characteristics in more detail. LES yields a compromise between computational efficiency of Reynolds averaged models (RANS) and the resolution of direct numerical simulations (DNS), all the while maintaining a wind field consistent with observational studies (Giometto et al. 2016). Entire CBDs can be resolved within the domain of the LES, and they can diagnose the characteristics of the near-source plume more finely than a Gaussian-assumed dispersion model would. Further, Gaussian plume models do not account for geometry within the urban canopy, meaning changes to this geometry would not be reflected in the suggested plume behavior from the Gaussian model.

This study aims to use an LES for scalar transport over complex terrain developed by Albertson (1996); Chamecki et al. (2008); Salesky et al. (2019) to quantify the relationship between urban geometry/source location and near-source plume moments. Philips et al.

(2013) performed a similar, idealized urban canopy study, but used a single domain with varying source locations and oblique wind angles to compare plume statistics. Here we consider the effects of separate urban geometries on higher order plume moments specifically.

In addition to the plume statistics, the behavior of instantaneous scalar concentrations is of great interest. Chamecki (2013) observed characteristics of velocity fluctuations, using the idea of persistence times (defined as interpulse period in Sreenivasan et al. (1983)) for quantifying the relationship between velocity perturbations within vegetative canopies. This study looks to relate the *scalar* fluctuation times to data-driven location in the domain, thereby describing local scalar concentration as a function of plume geometry. A relationship of this kind is key in determining the appropriate conditions for a Gaussian dispersion model, and when such assumptions may be invalid. By extension, describing this dispersion more accurately is imperative to alleviate risk of local exposure for potentially dangerous pollutants in urban regions.

1.2 Atmospheric Boundary Layer

The atmospheric boundary layer (ABL) is the lowest portion of Earth's troposphere, where frictional effects from the surface directly impact the characteristics of the atmospheric layer. Prandtl (1904) first described the concept of a fluid boundary layer, where the effects of friction are reserved for the fluid close to the surface of a stationary object. The ABL features intense diurnal variability tied to surface heat fluxes, but generally ranges from 1 - 2 km deep in the daytime convective boundary layer, to 100 - 200 m in the nocturnal stable boundary layer (Stull 1988). Figure 1.1 shows this evolution for an idealized homogeneous setting.

The ABL is the layer beneath the *free atmosphere*, which is largely separated from direct surface flux influences. In terms of internal structure, the ABL is often divided into two large sublayers, the inner and outer region. As the name suggests, the outer region

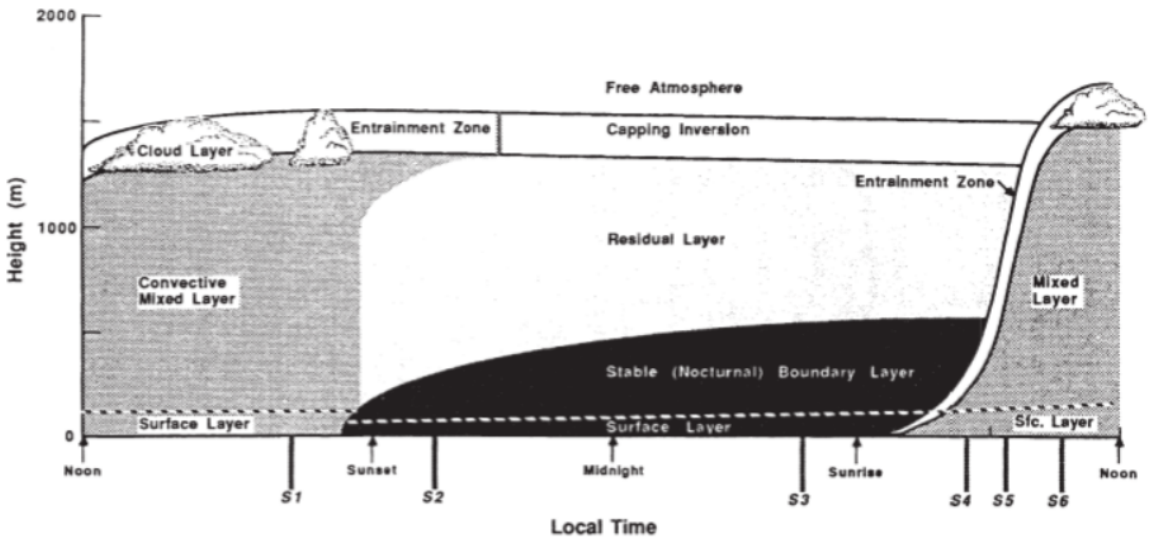

Figure 1.1: Diurnal variable of the ABL as portrayed by Stull (1988). Time is on the x axis and height is on the y axis.

is farther from the surface - where velocity and length scales separate from surface characteristics and include other features like the boundary layer depth (z_i). Conversely, the inner region contains much of the surface influences, including heat/moisture fluxes, and is where velocity and length scales are tied directly to the surface (like the friction velocity u_*). This often earns it the name surface layer in some literature. An important distinction with these subdivisions is that they are not separate — they overlap in a region known as the *inertial layer*. Closest to the surface is the roughness sublayer, where winds are independent of height and mechanical influences from the surface roughness elements are strongest. This sublayer extends from the surface to $2-5H$, where H is the mean height of the obstacles/roughness elements. Turbulence statistics cannot be simply scaled in this region due to fully three-dimensional flow directly impacted by the surface elements. The region below $z/H = 1$ is often called the canopy sublayer to distinguish itself as below the mean roughness element height. These layers typically evolve with the diurnal cycle, and adopt naming conventions resulting from the characteristics they acquire in this cycle. For

instance, the outer layer is also known as the convective or mixed layer during the day, and the residual layer at night.

1.2.1 Urban Boundary Layer

Urban canopies and add another layer of complexity to the ABL. The introduction of further mechanical mixing, spatial heterogeneity, and complex surface fluxes, lead to some distinct differences between an urban boundary layer (UBL) and more general ABL. Figure 1.2 highlights some of these differences, including many new sublayers tied to the urban canopy, a variable roughness length, and wake regions downstream of various obstacles. The urban canopy layer (UCL) is a additional sublayer designed to generalize the impact of obstacles within the larger UBL/ABL.

The transition from an ABL in a more rural region to a UBL is important in the context of atmospheric dispersion. The physical obstacles to flow entering an urban area lead to momentum transport of flow entering the urban canopy (Davidson et al. 1995; Bornstein 1987) and by extension any passive tracers within the flow. Due to large amounts of human activity, including fossil fuel burning and manufacturing, the UBL often contains large amounts of pollutants that cover a wide range of sizes, shapes, and states. One of the traditional ways of subdividing airborne pollutants is by using the particulate matter (PM) categories, which designate particles based on mean diameter (EPA 2018). The two most common subdivisions are PM_{10} and $PM_{2.5}$, referring to particles smaller or equal to 10 and 2.5 microns, respectively. Of particular concern is $PM_{2.5}$, which are small enough to pass through the alveolar–capillary barrier within the lungs, posing a risk to health for those with compromised respiratory/cardiovascular systems (Janssen et al. 2013; Chan and Lippmann 1980). A lesser known and regulated particulate class is the ultrafine particles (UFPs), which are smaller than either of the other categories and pose additional significant health issues; these are referred to as $PM_{0.1}$ in some literature (Schraufnagel 2020). An estimated

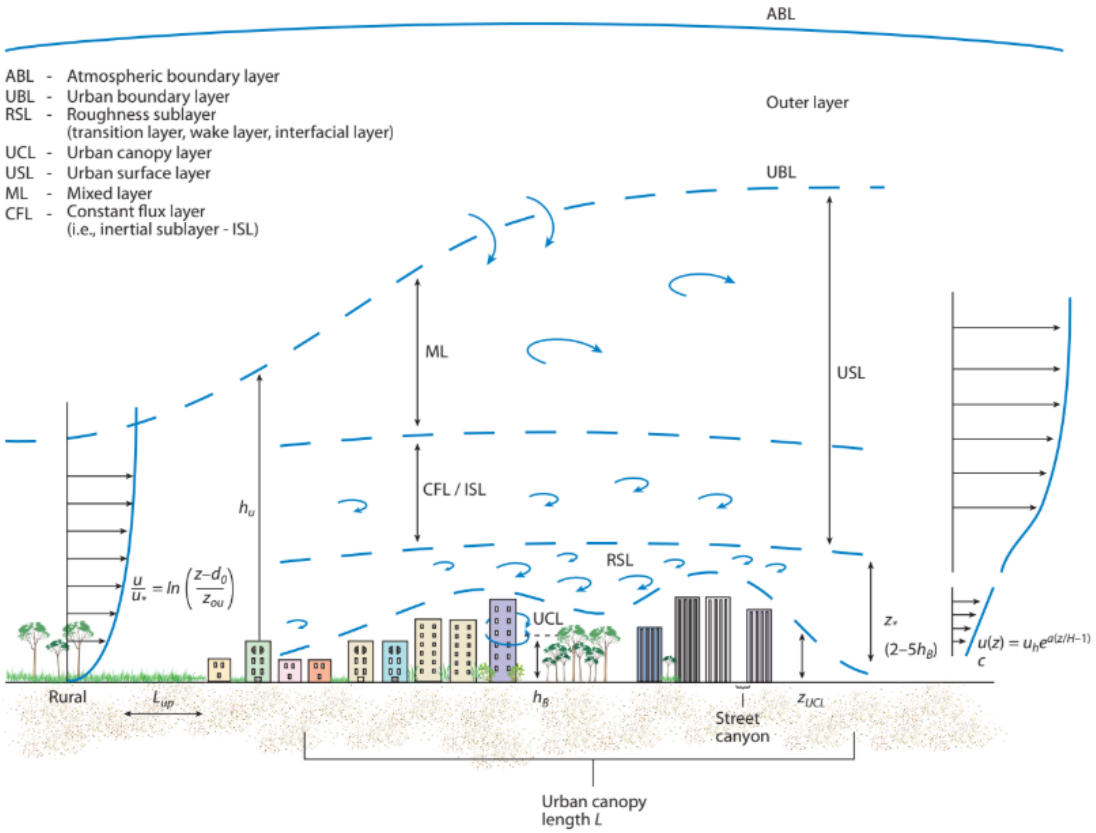

Figure 1.2: Assorted regions of the UBL - adapted from (Fernando 2010). Conventional logarithmic profiles using d and z_0 (displacement and roughness heights, respectively) and in-canopy profiles proposed by (Cionco 1965) are shown.

4.2 million annual premature deaths are attributed to exposure to particulate matter (WHO 2015).

Further, the global urban population is on the rise, putting more people under the influence of UBLs and urban pollutants. A 2018 UN report estimated 55% of the global population lives in urban areas, which is slated to increase to 68% by 2050 (UNDESA 2018). This means around 2.5 billion people will be added to urban areas within this time frame. The number of megacities (where a megacity is defined as having over 10 million people in its metropolitan area) is also on the rise — 33 were found in 2018 and 43 are expected by 2030. A greater understanding of particulate behaviour in an UBL is necessary to mitigate the elevated risk of health ailments for a ever-increasing metropolitan population.

1.3 Gaussian Dispersion Models

Plume models date back to pivotal works by Sutton and Simpson (1932) and Bosanquet and Pearson (1936), who developed some of the first theoretical analyses for atmospheric dispersion, despite not assuming a Gaussian fit for the plumes. Sutton returned to this topic some years later, when the threat of chemical warfare drove research for a deterministic dispersion solution in the lower atmosphere (Sutton 1947b). Sutton found deterministic equations for dispersion for a point source near the ground, resulting in a three-dimensional normal distribution of passive scalars downwind of the point source (Sutton 1947a), the first equations of their kind.

These normal or Gaussian solutions to atmospheric dispersion close the advection diffusion equation

$$\frac{\partial \overline{C}}{\partial t} + \nabla \cdot (\vec{U}\overline{C}) = D\nabla^2 \overline{C} \tag{1.1}$$

where $\overline{C}$ is mean concentration, $\vec{U}$ is the wind vector, and D is a turbulent diffusion coefficient (eddy diffusivity), a dynamic function of the turbulent flow. Closing this allows for the first deterministic solutions to dispersion in near surface atmosphere. However, many

features of the dispersion are heavily parameterized, including the diffusion coefficient itself.

Subsequent work on Gaussian models focused on expanding the base model from Sutton; Cramer (1957) derived a dispersion model that included standard deviations of the plume in both the horizontal and vertical (σ_y and σ_z respectively). Gifford (1961) and Pasquill (1961) helped finalize the Gaussian model as we understand it today by including stability parameters into the plume's dispersion. The result is the a Gaussian plume model for a near-ground constant source of passive scalars, here adapted from Seinfeld and Pandis (2006):

$$\overline{C}(x,y,z,H) = \frac{Q}{2\pi\overline{u}\sigma_y\sigma_z}\exp\left(-\frac{y^2}{2\sigma_y^2}\right)\left[\exp\left(-\frac{(z-H)^2}{2\sigma_z^2}\right)\exp\left(-\frac{(z+H)^2}{2\sigma_z^2}\right)\right] \quad (1.2)$$

where $\overline{C}$ is the time averaged concentration at a spatial location, Q is the strength of the continuous source in g/s or num/s, H is the source height, and $\overline{u}$ is the average x component wind speed at the source height. Spread in the horizontal and vertical are represented by σ_y and σ_z respectively. A visualization of this equation from Stockie (2012) is shown in Figure 1.3.

Interest in urban dispersion has fueled studies applying Gaussian models to the UBL as well. Briggs (1973) developed Gaussian parameters for plume heights as a function of terrain and stability characteristics; many of these parameters enjoyed widespread use in the past, often with misplaced execution (Griffiths 1994). Laboratory experiments have shown that these Gaussian models lay the appropriate framework for dispersion around idealized relatively short obstacles (Davidson et al. 1995; MacDonald et al. 1997; Macdonald et al. 1998). However, for more complex terrain and different source locations within the terrain, it is unclear how effective Gaussian models are at describing the entire plume, especially near the source. This is of particular interest to the current study.

Further, Gaussian models do not describe local exposure within the urban canopy. Pollutant exposure within the UBL, especially with passive scalar analogs like $PM_{2.5}$ and

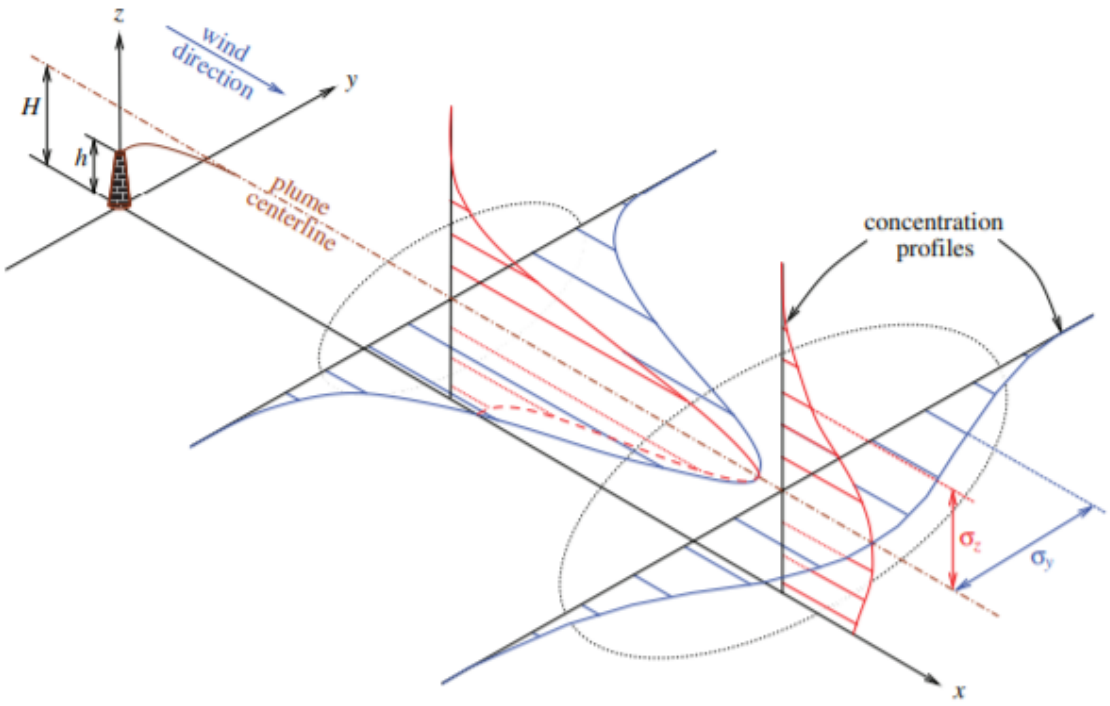

Figure 1.3: Schematic of a two dimensional plume from Stockie (2012). The dominate wind flow is in the x direction, leading to lateral and vertical spread of the plume denoted by σ_y and σ_z respectively.

PM_{10}, contribute to the previously mentioned cardiovascular and respiratory strain on at-risk individuals. Klein and Young (2011) used data from the Joint Urban 2003 experiment in OKC to describe sulfur hexaflouride concentration fluctuations in a CBD. Scalar fluctuations were found to be more significant along the edges of the plume rather than on the centerline itself. Zhou and Levy (2008) used the Operational Street Pollution Model (OSPM) developed by the National Environmental Research Institute (Berkowicz 2000) to calculate inhale fractions (iF) for a congested street canyon in Manhattan. The iF is defined by the fraction of material released from a source that is inhaled by a population. iFs were found to be orders of magnitude larger than predicted by regional-scale dispersion models, showing how high resolution near-source exposure statistics are crucial in mitigating risk for an urban population. Ng and Chau (2014) used a Reynolds-Averaged Navier-Stokes (RANS) model to test exposure for a suite of canyon configurations using the indirect exposure approach. Exposure was found to vary mostly as a function of prevailing wind/building configuration, but building setbacks could be effective at reducing personal exposure. These studies further emphasize the importance of high resolution urban dispersion modeling, especially through the lens of exposure statistics.

1.4 Large Eddy Simulations

Large Eddy Simulations (LES) are based upon a core premise - that the larger scales of a turbulent flow account for the majority of momentum/scalar transport. Following this principle, if a numerical simulation were developed to resolve these larger scales, and account for (i.e. model) the effects of smaller scales, than an accurate representation of a particular flow would be possible.

This proves advantageous from a computational standpoint - resolving only to a certain resolution of a flow requires significantly less calculations than a simulation resolving down to the smallest scales (i.e., Kolmogorov length scales) (Kolmogorov 1941). Pope (2000) demonstrated that the number of grid points needed in three dimensions scales with

the Reynolds number for a fully resolved model (i.e., DNS) by $\mathrm{Re}^{9/4}$. With atmospheric Reynolds numbers scaling at $\approx 10^7$, a DNS of the ABL is not currently possible with available computing clusters. As such, a coarser model allows for greater spatial coverage, leading to large domain sizes with fully characterized flow down to a dynamic/explicit spectral cutoff.

The LES equations of motion are derived by low pass filtering the Navier-Stokes equation, here recalled from Pope (2000):

$$\frac{\partial u_i}{\partial t} + u_j \frac{\partial u_i}{\partial u_j} = -\frac{1}{\rho}\frac{\partial p}{\partial x_i} + \nu \frac{\partial^2 u_i}{\partial x_j \partial x_j} \tag{1.3}$$

u_i is the velocity of the fluid for each component (i = 1,2,3), ρ is the density of the fluid, p is the pressure, and ν is the kinematic viscosity. Low-pass filtering results in the LES equation of motion

$$\frac{\partial \tilde{u}_i}{\partial t} + \tilde{u_j}\left(\frac{\partial \tilde{u}_i}{\partial x_j} - \frac{\partial \tilde{u_j}}{\partial x_i}\right) = -\frac{1}{\rho}\frac{\partial \tilde{p}}{\partial x_i} - \frac{\partial \widetilde{\tau_{ij}}}{\partial x_j} \tag{1.4}$$

here recalled from Kumar et al. (2006). $\tilde{u_i}$ is the resolved velocity component in each direction, $\tilde{p}$ is the resolved dynamic pressure term, and $\widetilde{\tau_{ij}} = \widetilde{u_i u_j} - \widetilde{u}_i \widetilde{u}_j$ is the deviatoric part of the sub-grid scale (SGS) stress tensor. A resolved quantity (denoted by the˜) refers to the low-pass filtered variable to the grid spacing Δ. The SGS stress term is a manifestation of the turbulent closure problem and needs to be parameterized in order for the equation to close properly. Smagorinsky (1963) proposed the following parameterization:

$$\tau_{ij} = -2(C_s\Delta)^2 |\tilde{S}| \tilde{S_{ij}} \tag{1.5}$$

where C_s is the Smagorinsky coefficient, $\Delta = (\Delta_x \Delta_y \Delta_z)^{1/3}$ is the filter width, and $|\tilde{S}| = \sqrt{2\tilde{S_{ij}}\tilde{S_{ij}}}$ where $\tilde{S_{ij}} = \left(\frac{\partial \tilde{u_i}}{\partial x_j} + \frac{\partial \tilde{u_j}}{\partial x_i}\right)$. Lilly (1967) applied the Smagorinsky closure to LES more formally by finding an analytical solution for C_s based on a specified spectral cutoff filter. Deardorff (1972) applied this work to the atmosphere, using a finite-differencing LES to study a unstable ABL with aspects of Monin-Obukhov similarity theory (Monin and Obukhov 1954). These studies, combined with rapidly expanding computational power, facilitated widespread advances in various aspects of LES in the coming years, including

mixed psuedo-spectral and finite differencing momentum equations (Moeng 1984), and dynamic SGS models that better capture complex flows (Germano et al. 1991). Dynamic SGS models calculate C_s from the resolved scales as the simulation is running, ensuring proper representation of turbulent flows from the resolved to the sub-grid scales. An explicit Smagorinsky coefficient throughout a domain make maintaining this balance in the presence of significant spatial heterogeneity and complex flows challenging.

1.4.1 Urban LES Studies

The complexity of urban canopies makes LES of the UBL significantly more challenging than a comparable homogeneous setting. However, those same complexities are magnified in field experiments, where sensitive measurement systems make empirical data challenging to measure properly (Pardyjak and Stoll 2017) or determine representative statistics from (Klein and Young 2011). Observations in urban settings also tend to be focused on a single tower, and time-averaged statistics from these towers, which are not necessarily indicative of spatial averages within the neighborhood. Figure 1.4 shows some of these discrepancies; note the differences between tower measurements and results from the LES. While the LES is within the error bars for the tower measurements, the discrepancy is large enough to where flow characterization from the tower data is difficult, especially when geometry is considered a variable like the present study.

An idealized LES can provide the necessary 3D fields to fully characterize an urban flow. With the added flexibility of variable geometry and virtual tower data, this makes it a very attractive option for studying turbulent flow and dispersion in a urban canopy.

Typical idealized LES studies take the form of street canyons (Walton and Cheng 2002; Cui et al. 2004) or a grid of cuboids (Kanda et al. 2004; Philips et al. 2013). Studies often explore the relationship between urban geometry and mean momentum and scalar statistics (Xie and Castro 2008; Hayati et al. 2017). Recent advances have facilitated incorporation

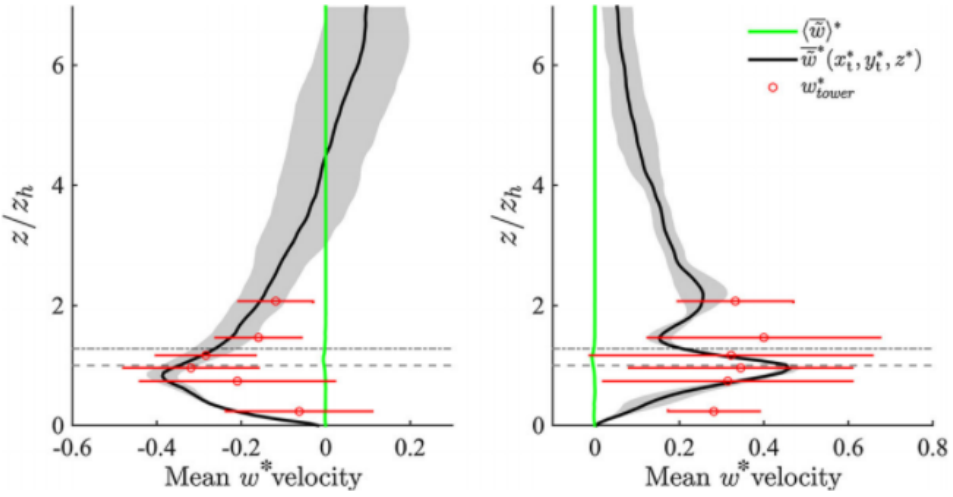

Figure 1.4: Adapted figure from Giometto et al. (2016). Separate along-canyon and cross-canyon simulations are shown on the left and right respectively. Double-averaged and temporally averaged vertical velocity components from the LES are shown, with the data coming from the tower location in the domain. Tower data is given by the red error bars. Normalized height is on the *y* axis and the mean vertical velocity is on the *x* axis.

of more realistic terrain into LES by using LIDAR data with an immersed boundary method (IBM) (Bou-Zeid et al. 2009; Giometto et al. 2016, 2017).

Tseng et al. (2006) used an IBM to simulate scalar point-source urban dispersion in urban canopies. While much of this work focused on properly discritizing the domain to capture obstacles, evidence of flow channeling around buildings and spatial variability of scalars was found. Probability Density Functions (PDFs) of concentration were created at various downstream locations in a urban environment emulating downtown Baltimore, MD; these results are shown in Figure 1.5. Significant spatial and temporal variability in concentration is evident, and the PDF indicates that distributions are greatly affected by location. The authors suggest that this LES probabilistic framework could be expanded to extreme exposure events and turbulence statistics as a whole. With a focus on domain/plume location, the current study will explore these statistics amply, providing further authentication of LES as a viable pollutant dispersion tool.

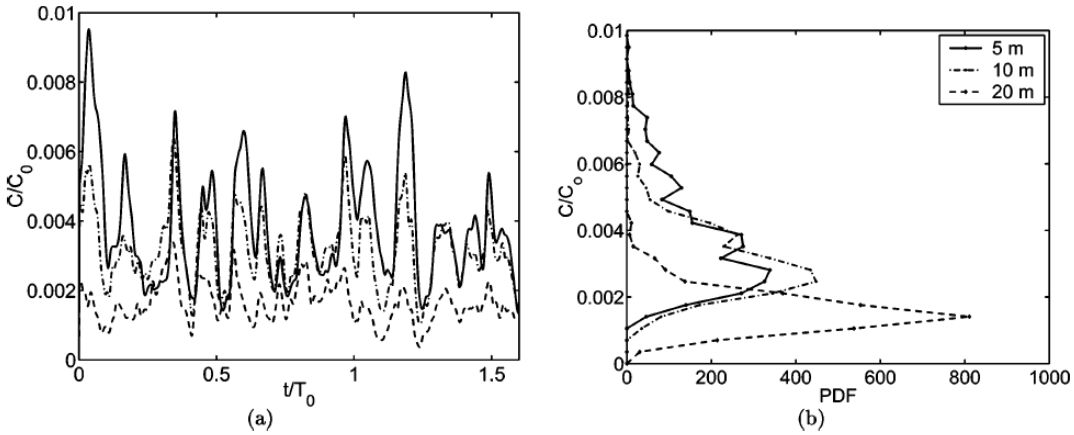

Figure 1.5: Adapted figure from Tseng et al. (2006). Timeseries (a) and Probability Density Function (b) of normalized concentration at a downstream location from two point-sources. Various heights at this location are denoted by line type. Concentration on both plots is normalized by $C_0 = u^*/Q$ where u^* is the friction velocity and Q is the source strength.

Santos et al. (2019) used an LES to prescribe peak-to-mean concentration ratios in an urban environment. Concentration output was compared to a power-law exponent relating maximum to mean concentration values, but the sensitivities of the exponential model meant that the results were notably dependent on the SGS model used. These ratios are not explored in the present study in favor of describing exposure as a function of geometry/spatial location.

One of the closer analogs for this study was done by Philips et al. (2013), who used a staggered vertical grid with increasing resolution close to the lower boundary of idealized cuboids. Cuboid distributions were tested in a suite of simulations testing point-source passive scalar emission at various locations in the domain. Figure 1.6 shows the distribution of cuboids for a given simulation. A finite volume solver with nonuniform cell size and a boundary fitted mesh is used to solve the momentum equations in both the horizontal and vertical (Mahesh et al. 2004). Staggered, skewed and aligned cuboids were tested by adjusting the angle of the mean gradient pressure forcing.

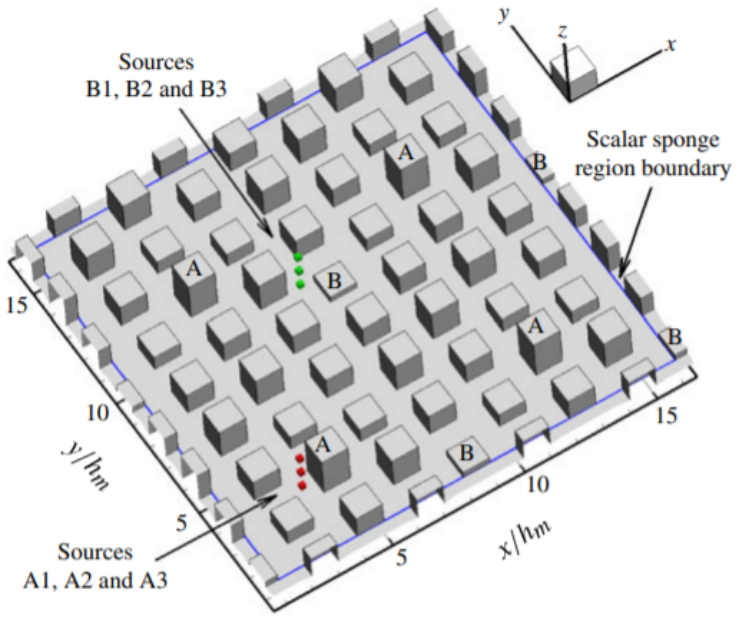

Figure 1.6: LES domain used by Philips et al. (2013). Various source locations are shown, and were placed near the tallest and shortest mode of cuboid (A and B, respectively).

Grid resolution was only shown to have minor implications toward momentum statistics in the flow, with the largest discrepancy in streamwise momentum fluxes. Results from the plume simulations showed a relationship between vertical/horizontal spread of the scalar plume and arrangement of the cuboids relative to wind flow; these results are shown in Fig. 1.7. Horizontal plume spread was found to vary slightly as a function of source height, but vertical plume spread did not vary significantly between each of the simulations. Many of these findings were supported by observational studies with cuboids (Belcher 2005; Belcher et al. 2015), further validating LES as a potent urban dispersion tool. While Gaussian plume parameters are calculated and compared based on source location, a relationship between higher order scalar plume moments (i.e., skewness and kurtosis) and the urban geometry has not been explored previously from LES. Combined with a lack of spatial dependence in urban LES studies that describe exposure, and this provides the motivation for the current study.

1.5 Research Questions

In an effort to address understudied aspects of urban dispersion with LES, this thesis will focus on answering a few focal questions, namely

1. To what extent does urban geometry and scalar source location affect near-source plume moments for passive scalar dispersion?

2. To what extent does location in the plume/domain affect local exposure to a passive scalar above a certain threshold?

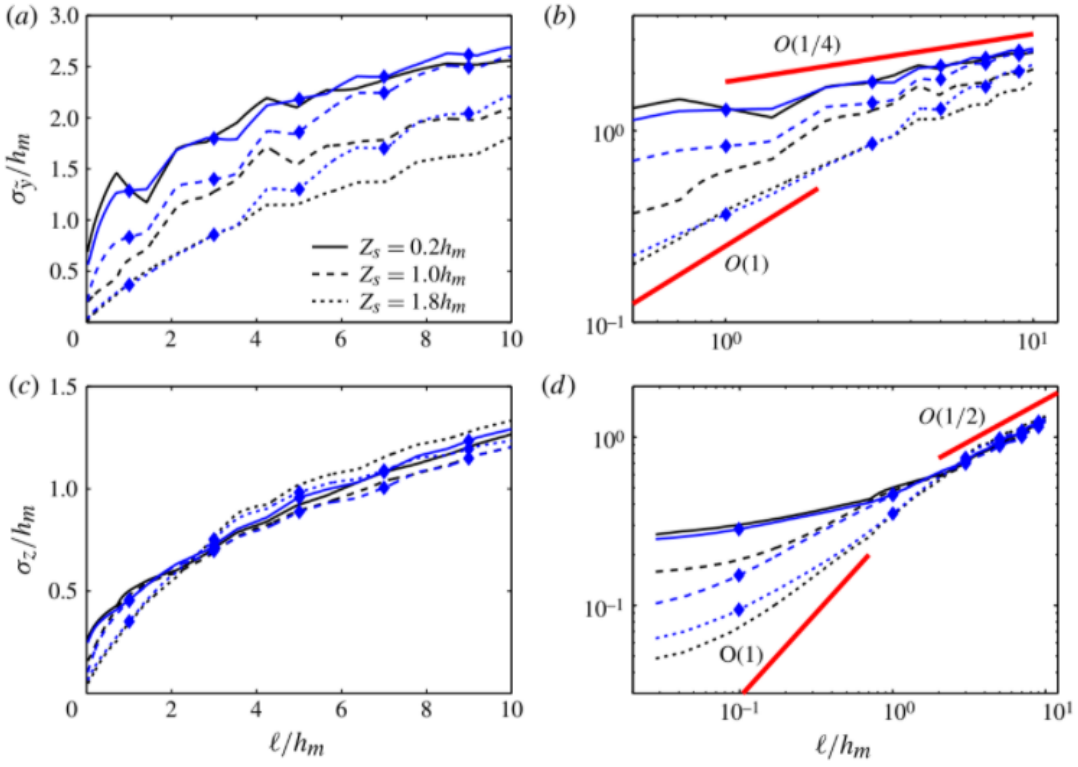

Figure 1.7: Adapted figure from Philips et al. (2013). Source locations are denoted by the black and blue lines, which correspond to locations A and B in Figure 1.6 respectively. Normalized distance downstream of the source is on the x axis, and source height is given by line type. Plume width (equivalent to second plume moment) for the horizontal and vertical are the top and bottom panels respectively, with a linear and log-log scale for each on the left and right panels respectively.

Chapter 2

Methods

2.1 Overview of Large Eddy Simulation

The LES code used for this thesis traces its origins to John Albertson's PhD dissertation (Albertson 1996). The filtered 3D momentum equation is given by Equation 1.4, recalled again here for convenience

$$\frac{\partial \tilde{u}_i}{\partial t} + \tilde{u_j}\left(\frac{\partial \tilde{u}_i}{\partial x_j} - \frac{\partial \tilde{u_j}}{\partial x_i}\right) = -\frac{1}{\rho}\frac{\partial \tilde{p}}{\partial x_i} - \frac{\partial \widetilde{\tau_{ij}}}{\partial x_j} \tag{2.1}$$

The Coriolis and buoyancy terms are not included because we are focusing on neutrally stratified, neighbourhood-scale plume characteristics. Equation 2.1 is solved using pseudo-spectral horizontal derivatives and second order finite differencing for the vertical derivatives (Albertson and Parlange 1999). As discussed in Section 1.4, the SGS stress tensor needs to be modelled for proper turbulent cascade into the sub-grid scales. A Lagrangian scale-dependent dynamic SGS model is used for this (Bou-Zeid et al. 2005), which follows Smagorinsky's paramterizaton in Equation 1.5, and uses a dynamic approach found in Lilly (1992) to average over Lagrangian fluid trajectories to more accurately estimate C_s (Meneveau et al. 1996). This method results in more accurate SGS representation in the near-wall region, which is especially important for complex flows like UBLs. A fully-explicit second-order Adams-Bashforth scheme is used for time integration.

Over flat, neutrally stratified, horizontally homogeneous terrain, the logarithmic law of the wall (i.e., log-law) is typically used as a lower boundary condition in LES. The log-law states that the mean velocity of a turbulent flow is proportional to the logarithm of the normal distance from the fluid to the wall. Here we recall this from Pope (2000):

$$u^+ = \frac{1}{k}\ln y^+ + C \tag{2.2}$$

where $u^+ = \frac{\langle U(t) \rangle}{u_*}$, k is the von Karman constant typically taken as ≈ 0.4, y^+ is distance from the wall normalized by the viscous length $\frac{\nu}{u_*}$, and C is a constant. The brackets $\langle\rangle$ refer to a horizontal spatial average. Kumar et al. (2006) defined the wall stress in LES using the log-law by defining it as a function of u_* and using the first grid cell above the surface for time averaged statistics. However, for horizontally heterogeneous terrain like an urban canopy, a separate approach must be taken because the spatially dependent wall stresses. The immersed boundary method (IBM) is employed here to represent the complex surface (Mittal and Iaccarino 2005). This IBM uses a level set function, which is a signed distance function that yields normal distance (φ) from the immersed surface, applying the log-law in a banded region within a certain range of positive φ values (Chester et al. 2007). The IBM approach is preferred to terrain following coordinates (Gal-Chen and Somerville 1975) due to its flexibility with abruptly shaped surfaces like cuboids or buildings. In addition, all of the boundary interface is still accounted for on a Cartesian grid, meaning the computational overhead is substantially lower than domains with more complicated or unstructured grids. The IBM also adds a forcing term to the right hand side of Equation 2.1 to force zero velocity at the fluid-solid interface. A detailed overview of this method is found in Salesky et al. (2019).

For passive scalar transport, an Eulerian finite volume solver is employed, with a Cartesian cut-cell method to account for the domain geometry. An Eulerian approach here is helpful in reducing the computational expense for a large amount of scalars in the domain. The result is particle evolution modelled by the advection diffusion equation:

$$\frac{\partial \tilde{C}}{\partial t} + \tilde{u} \cdot \nabla \tilde{C} = -\nabla \cdot \pi^C + Q_{src} \tag{2.3}$$

where $\tilde{C}$ is the filtered or resolved particle concentration field, $\tilde{u}$ is the resolved velocity field, π^C is the SGS particle concentration flux, and Q_{src} is the source term. A detailed overview of the SGS particle flux model is found in Salesky et al. (2019). A third-order bounded upwind advection scheme is used for transport (Gaskell and Lau 1988) that prevents negative concentrations, and velocity interpolation to finite volume faces is conserved

(Chamecki et al. 2008). The Cartesian-cut cell method discretizes each of the finite volume faces to fit the immersed surface where it intersects grid cells, and appropriate adjustments to the volume and area fraction of each cell are made to maintain particle conservation in the resulting irregularly shaped cut-cells (Mittal and Iaccarino 2005; Salesky et al. 2019) Because we are interested in scalars less than or equal to 2.5 microns in diameter, particle momentum and deposition are not accounted for in this study because these particles can be treated as passive scalars without appreciable loss in generality.

2.1.1 Parameter Space

Two different idealized urban canopies are used in this study. Both feature 96 cuboids in a domain size of 240x160x80m, with each of the cuboids measuring 10x10x10m at the bottom of the domain. There are twelve cuboids in the x direction, and eight in the y direction. One of the geometries places each successive row of cuboids in the same lateral location as the previous, leading to aligned street canyons oriented in both y and x. The other geometry offsets each successive row by one full building width, presenting a staggered appearance while maintaining canyons in y. These geometries are shown in Figure 2.1

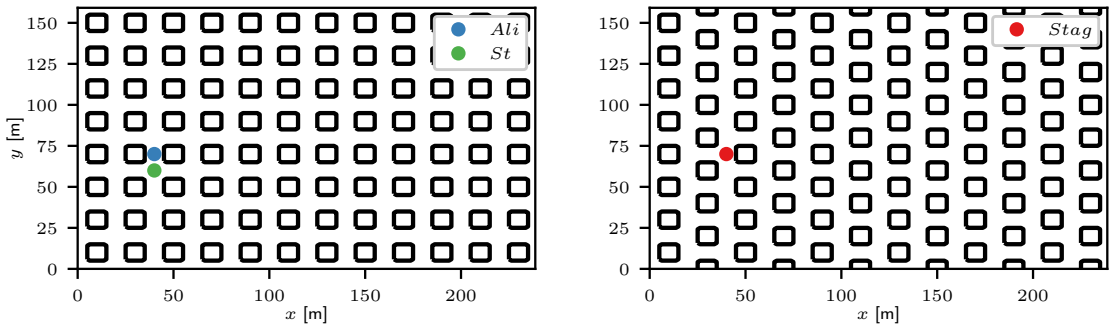

Figure 2.1: Comparison of aligned and staggered urban geometry, respectively. Source locations are shown for reference.

Each of the cuboids has a 1% slope to avoid issues with the level set building correctly. A half channel simulation is used to represent a turbulent flow over the urban canopies - the domain covers half of the channel and applies the zero boundary condition (BC) at the top of the domain. A mean pressure gradient force (PGF) is used to create the wind flow, and periodic BCs for momentum are used horizontally to emulate an infinite array of the urban canopy. For scalars, inflow-outflow conditions are used, which removes scalars from the simulation that exit the domain; this is key in diagnosing a single, point-source plume. The PGF is only imposed in the x direction to ensure that any lateral spread with the scalars is due to the geometry of the domain and the resulting turbulent fluxes. For this reason, distances in x and y are used interchangeably with streamwise and spanwise, respectively. In order to ensure the lower boundary condition is consistent throughout the domain, the IBM was raised two meters from the bottom of the computational domain. As a result, the top of the cuboids rests at $z = 12$m, and the bottom of the street canyon is at $z = 2$m. This ensures that multiple grid points below the immersed surface are able to impose the lower BC ubiquitously. Vertical distances henceforth will be considered from the bottom of the street canyon rather then from the bottom of the computational grid.

Before testing with passive scalars, grid convergence tests were performed in order to determine the proper numerical discretization for the urban canopies. Five different grids were tested: $\{N_x \times N_y \times N_z\} = 96^3, 128^3, 160^3, 192^3$, and 224^3. Momentum statistics were calculated for each of the otherwise identical simulations, which ran for approximately $18T_l$, where $T_l = L_z/u_*$ is the large eddy turnover time, L_z is the domain height, and u_* is the friction velocity defined as

$$u_* = \sqrt{|\langle \overline{u'w'} \rangle|_{max}} \tag{2.4}$$

where $\overline{u'w'}$ is the covariance of the streamwise and vertical velocity fluctuations. The overline refers to a temporal average. The results from these tests are shown in Figure 2.2.

The streamwise and spanwise velocity variances, in panels a) and b) respectively, peak just above the building height at $z/H \approx 1.5$, although significant spanwise variance is noted

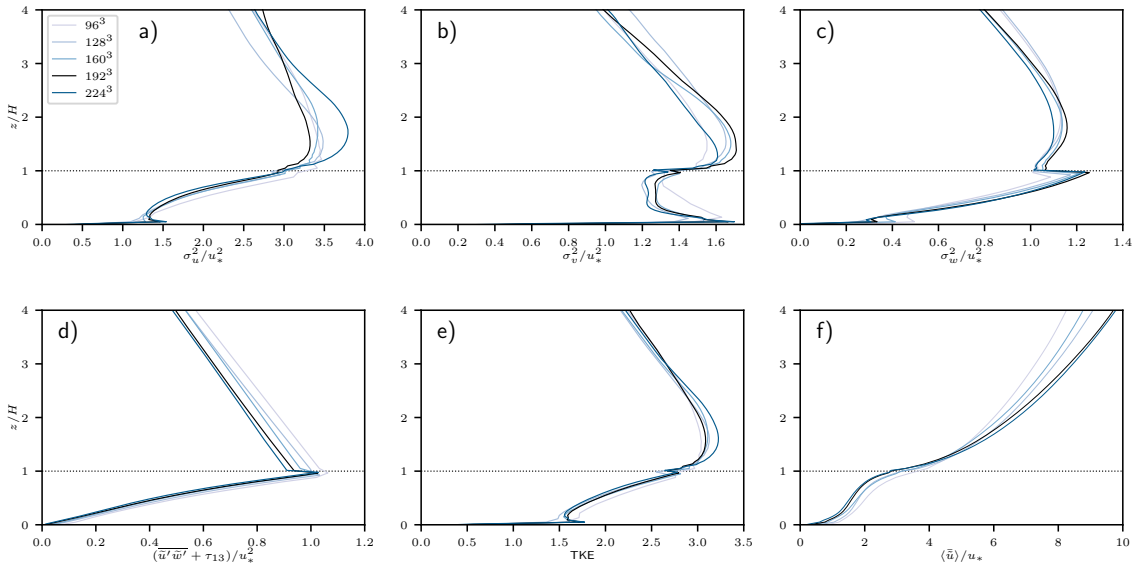

Figure 2.2: Various turbulence statistics compared at different numerical discretizations. Panels a), b), and c) show the horizontally averaged resolved velocity variance for the streamwise, spanwise, and vertical velocity components, respectively. These variances are all normalized by the friction velocity squared. Panel d) shows the combination of the resolved stresses and contribution from the SGS. Panel e) shows the horizontally averaged turbulent kinetic energy (TKE) of each flow. Panel f) shows the normalized temporal and spatially averaged streamwise velocity. Vertical distance is normalized by building height H. The 192^2 simulation is highlighted in black to better highlight the discretization of choice. The top of the buildings is marked by the dotted black line at $z/H = 1$

near the lower boundary. Vertical velocity variance in panel c) reaches its peak around the top of the cuboids. Minor dependence on resolution is noted for the individual resolved momentum variances in panels a),b) and c). Panel f) shows agreement with the two highest resolution members about the RSL velocities. The maximum stress region near the top of the buildings $z/H \approx 1$ is clear on Panel d). Panel e), where TKE $= \frac{1}{2}[\overline{\widetilde{u}'\widetilde{u}'}^2 + \overline{\widetilde{v}'\widetilde{v}'}^2 + \overline{\widetilde{w}'\widetilde{w}'}^2]$, shows the net differences in each resolution for the momentum variances. It is not clear how to incorporate the SGS features (i.e., $\widetilde{u_i u_i} - \widetilde{u}_i\widetilde{u}_i$) into these variances, so only the resolved scales are shown here with the exception of the stresses. 224^3 is a slight outlier in the region just above the building height, largely due to its much higher resolved streamwise velocity variance in panel a). This is similar to the discretization findings in Philips et al. (2013). However, with appreciable convergence below $z/H \approx 1$ for the TKE, and excellent agreement between 192^3 and 224^3 in Panel f), 192^3 is an excellent compromise between the statistics of 224^3 and the computational expense of the lower resolution tests. Therefore, 192^3 was chosen as the optimal resolution moving forward into the scalar simulations, and will be the default numerical discretization unless otherwise stated.

In order to properly capture plume behavior, the passive scalar source location needs to be sufficiently upstream from the downstream edge of the domain, while maintaining appropriate distance from the upstream boundary condition. The lateral street canyon centered on $x = 40$m was therefore chosen for the streamwise point-source location. In terms of lateral location, three different cases for the source location are used; the first two place the source behind the cuboid centered at $y = 70$m within the staggered and aligned canopy respectively. The third places the source in the street canyon oriented along $y = 60$m within the aligned canopy. This was done to reveal any differences in scalar plume behavior resulting from domain placement in addition to CBD structure. These source locations are shown in Fig. 2.1.

For both of the urban geometries, momentum simulations were run for $\approx 25T_l$ to create a well-developed flow. Simulations with continuous point-source scalar emission were

then run for each of the three cases, with the well-developed simulations providing the initial momentum conditions. Table 2.1 highlights the specific parameters used for these simulations. We define the advective plume timescale as

$$T_a = \frac{L_x - x_{src}}{\overline{u_H}} \tag{2.5}$$

where $L_x - x_{src}$ is the distance from the streamwise source location to the downstream boundary condition at $L_x = 240$m, and $\overline{u_H}$ is the mean streamwise velocity at $z/H = 1$. This is preferred over T_l because we want to ensure independent samples of the plume are captured with the timescale. T_a differed slightly with each geometry due to different mean wind speeds, but approximately $18T_a$ were used for each simulation. Three different source heights were tested for each of the three source cases, resulting a suite of nine simulations. Each source location is described in Table 2.2.

Table 2.1: Overview of computational parameters used for the plume moment simulations. dt is the computational timestep, Q_{src} is the point source strength is number of particles per second, $\{N_x \times N_y \times N_z\}$ is the numerical discretization, $\{L_x \times L_y \times L_z\}$ is the domain size, and $\Delta x, \Delta y, \Delta z$ is the approximate grid spacing in each direction.

Parameter	Value
dt	0.0005
nsteps	300000
T_a	6.5-8.2 sec
Q_{src}	3000 #/s
$\{N_x \times N_y \times N_z\}$	192^3
$\{L_x \times L_y \times L_z\}$	240x160x80m
$\Delta x, \Delta y, \Delta z$	1.25, 0.83, 0.416 m

Table 2.2: Overview of source locations for each configuration. Coordinates are given in meters.

		x_{src} [m]	y_{src} [m]	z_{src} [m]
Aligned (*Ali*), Staggered (*Stag*)	low	40	70	0.5
	mid	40	70	4.25
	high	40	70	10
Aligned In-Street (*St*)	low	40	60	0.5
	mid	40	60	4.25
	high	40	60	10

2.2 Plume Moments

An objective means of comparing the scalar plumes from simulation to simulation was needed. Previous studies have shown that plumes become near Gaussian far enough from the source (Davidson et al. 1995; MacDonald et al. 1997; Macdonald et al. 1998), so an easy comparison to a perfectly Gaussian plume is also needed. This makes plume moments the ideal framework to diagnose the plume characteristics in our urban canopies, especially in the near-source region. Scalar plume moments were calculated for both the 2D plumes downstream of a point source, much like is shown in Figure 1.3. The first lateral moment is given by

$$\mu_y(x) = \frac{\int_{-\infty}^{+\infty}\int_{0}^{+\infty} y\overline{C}(x,y,z)dzdy}{\int_{-\infty}^{+\infty}\int_{0}^{+\infty} \overline{C}(x,y,z)dzdy} \tag{2.6}$$

where y is the spanwise location, μ_y is the lateral plume centerline, and $\overline{C}$ is the time-averaged scalar concentration for a given grid cell. Higher order moments are given as

$$M_y^n(x) = \frac{\int_{-\infty}^{+\infty}\int_{0}^{+\infty} (y-\mu_y(x))^n\overline{C}(x,y,z)dzdy}{\int_{-\infty}^{+\infty}\int_{0}^{+\infty} \overline{C}(x,y,z)dzdy} \tag{2.7}$$

where n referes to the nth moment ($n = 2 = \sigma^2, n = 3 \approx S_k, n = 4 \approx K$), and μ_y is the lateral centerline from Equation 2.6. Vertical moments are the same with the vertical coordinate weighted in the numerator:

$$\mu_z(x) = \frac{\int_{-\infty}^{+\infty}\int_{0}^{+\infty} z\overline{C}(x,y,z)dzdy}{\int_{-\infty}^{+\infty}\int_{0}^{+\infty}\overline{C}(x,y,z)dzdy} \tag{2.8}$$

$$M_z^n(x) = \frac{\int_{-\infty}^{+\infty}\int_{0}^{+\infty}(z-\mu_z(x))^n\overline{C}(x,y,z)dzdy}{\int_{-\infty}^{+\infty}\int_{0}^{+\infty}\overline{C}(x,y,z)dzdy} \tag{2.9}$$

For the second moment, the square root of $M_{y,z}^2(x)$ yields the standard deviation of the plume. The skewness and kurtosis are normalized by $\sigma^{n/2}$. These separate horizontal and vertical plume moments for each simulation characterise the fully three-dimensional plume using only line representations. An example of time-averaged concentration overlaid with select plume moments is shown in Figure 2.3.

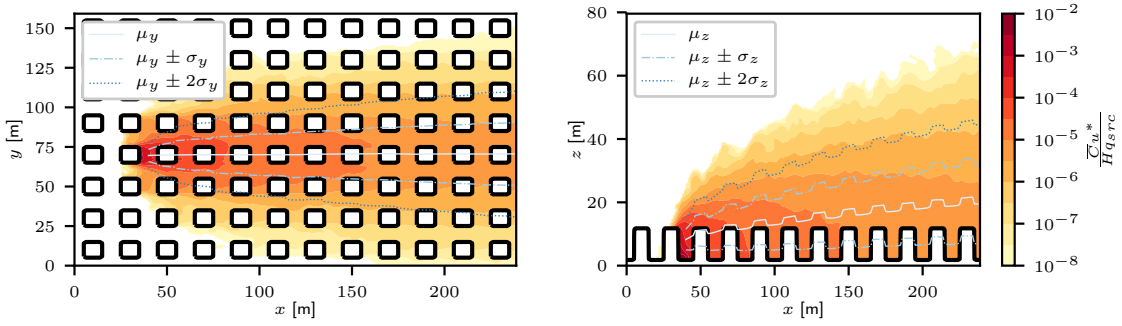

Figure 2.3: Cross-sections of time-averaged concentration for a well-developed plume. The left panel shows a cross-section with height fixed at source height; the right panel shows a cross-section with lateral distance fixed at y_{src}. Appropriate horizontal and vertical moments are shown for the horizontal and vertical slices respectively. Time averaged concentration is show on a log-scale,and normalized by the friction velocity u_*, source height H, and source strength q_{src}.

For the spanwise plume moments, the mean centerline remains relatively constant with streamwise distance, but spread about that mean increases with the same distance. The spanwise velocity flux due to the cuboids significantly aids in this spread. For the vertical

moments, the mean centerline slowly increases in height with streamwise distance; as more and more scalars reach higher into the domain, the center of mass will slowly rise. Similar effects are seen with the vertical plume spread. Note the oscillatory nature of the mean centerline - when the centerline is above a street canyon, there are more scalars lower in the domain compared to when the centerline is above a cuboid, leading to a quasi-terrain-following plume moment.

2.3 Instantaneous Towers

A method of quantifying instantaneous exposure to scalars is necessary due to the importance of population exposure. Plume moments are best at diagnosing general plume behavior within an urban canopy, but for describing local concentration fluctuations in the interest of human health, a separate approach must be taken. Virtual towers were placed in the domain that yield momentum and scalar variables at each timestep and each vertical grid cell. Towers were placed in a grid at regions dictated by the completed plume moment simulations; three towers were placed along μ_y when the vertical centerline μ_z reached $1.25H, 1.5H$, and $2H$, where H refers to the height of the cuboids. Three more towers were placed at $+2\sigma_y$ at the same streamwise location as the first three towers, resulting in a grid of six towers downstream from the source location. Three additional towers were placed at $-2\sigma_y$, but these data were not considered on the basis of plume symmetry in the lateral direction. While this theoretically results in different tower locations for each type of geometry/setup, the data-driven approach was favored over set tower locations independent of geometry because any behavior with the exposure statistics will therefore be a property of the geometry alone, and not adjustments to the plume moments relative to the fixed towers. Raw tower locations given by the moments were then subjectively moved into the nearest street canyon to best capture the ground level statistics. The final result is a group of six towers capturing instantaneous filtered variables through the vertical extent of the domain,

three along the plume moment centerline, and three along the $+2\sigma_y$ moment. For simplicity, these towers are used interchangeably with cardinal directions in their general vicinity when viewing the domain from the top down perspective, with positive x to the right. An illustration of this process is shown in Figure 2.4.

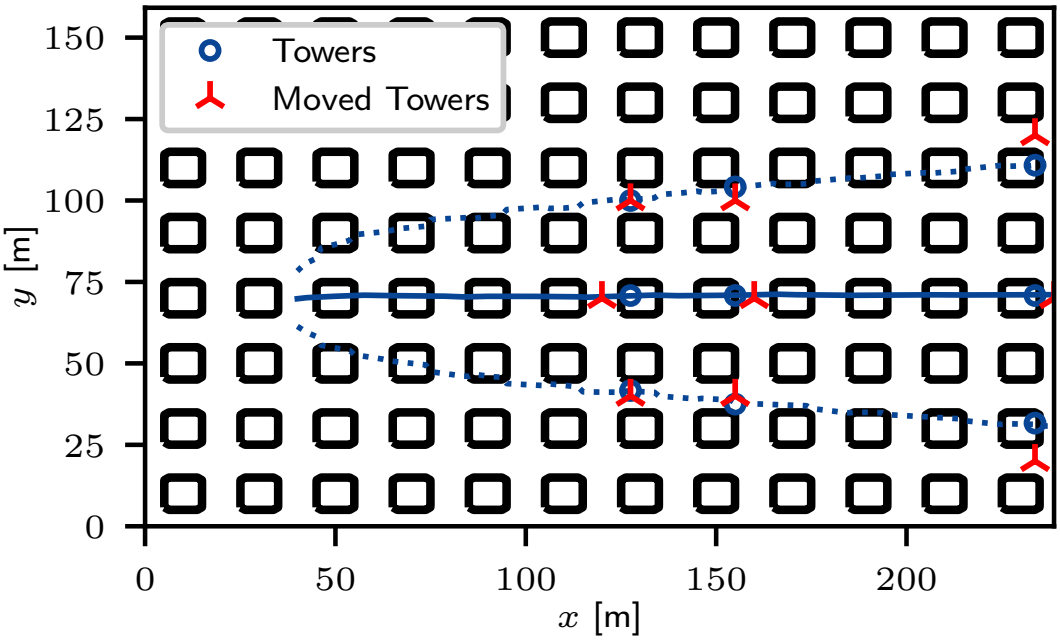

Figure 2.4: Depiction of tower locations on the medium density, aligned geometry setup. The solid line is the lateral plume centerline from the moment calculations, and the dotted lines represent the $\pm 2\sigma_y$ of the same plume. Pure data driven tower locations are shown by the blue circles; the moved tower locations shown in with the red crosses. The tower in the top right is the "northeast" tower, followed by (counterclockwise from that tower) north, northwest, west, center, and east towers. The three towers at the bottom of the domain along $-2\sigma_y$ are not used.

Concentration probability distribution functions (PDFs) were created for each tower location, and PDFs of exposure to fluctuations above some threshold were calculated. This

will yield information about not only the distribution of concentration locally, but also characterize how long concentration remains above some arbitrary threshold. These exposure statistics were calculated by using an exceedance principle. For a given tower, concentration values are given for each timestep of the simulation at each vertical level of the tower. Time averaged concentration values were found for each level, along with standard deviations. A threshold was set at some fixed number of standard deviations above the mean, and exceedance times were found for each event that crossed this threshold. This allows each vertical level of the tower to approach a probability distribution function (PDF), provided there is sufficient data to sample. Chamecki (2013) used this notion of exceedence by analysing the velocity fluctuations in a plant canopy using LES; in this study the *concentration* fluctuations are the focus. An illustration of exceedence on a timeseries of concentration is shown in Figure 2.5

These exposure statistics do not converge as quickly as the integral statistics found in the plume moments. To avoid individually long simulations and to better control the amount of data needed, an ensemble approach was taken here by adjusting the noise generator at the start of the simulations. The initial condition module uses a random number generator based on a user submitted integer to generate the noise needed for the turbulent flow to develop. Changing this integer will not affect temporally averaged turbulence or scalar statistics, but will provide different instantaneous momentum/scalar values throughout the domain, creating independent tower samples that emulate longer simulations. The tower statistics are found by combining each ensemble member into a larger sample space; each ensemble runs with only momentum for $\approx 10T_l$ to create a well developed flow, before scalars are released and run for an additional $\approx 15T_l$. An example of tower ensemble concentration is shown in Figure 2.6. The momentum spin-up is denoted by the zero concentration period up to about 80 seconds. Scalars are first released from the upstream location at 75 seconds, but sampling at each tower is not done until 95 seconds to ensure that scalars are well established throughout the domain, including the most downstream

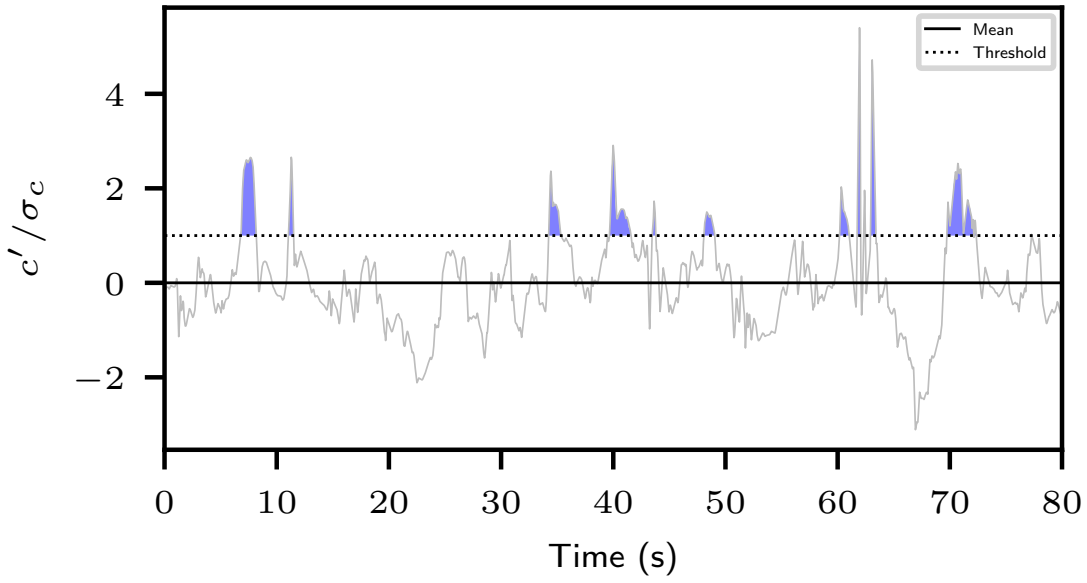

Figure 2.5: Example timeseries of instantaneous concentration from an ensemble member. Normalized concentration is shown on the y axis, while time is on the x axis. $\pm 1\sigma_c$ is denoted by the dotted black line, and is used as the threshold for exposure times. Time above the threshold is shaded, and would contribute to a distribution of exposure times for each individual event. The sampled height is at 1.75 meters above the street $N_z = 9$ or $z/H = 0.175$

towers. This time period from 95 seconds ($t = 190000\Delta t$) to the end of the simulation are the portions stitched together between the ensembles to emulate the longer simulations. A total of eight ensembles are used for this study, with the medium density, aligned cuboids as the geometry of choice.

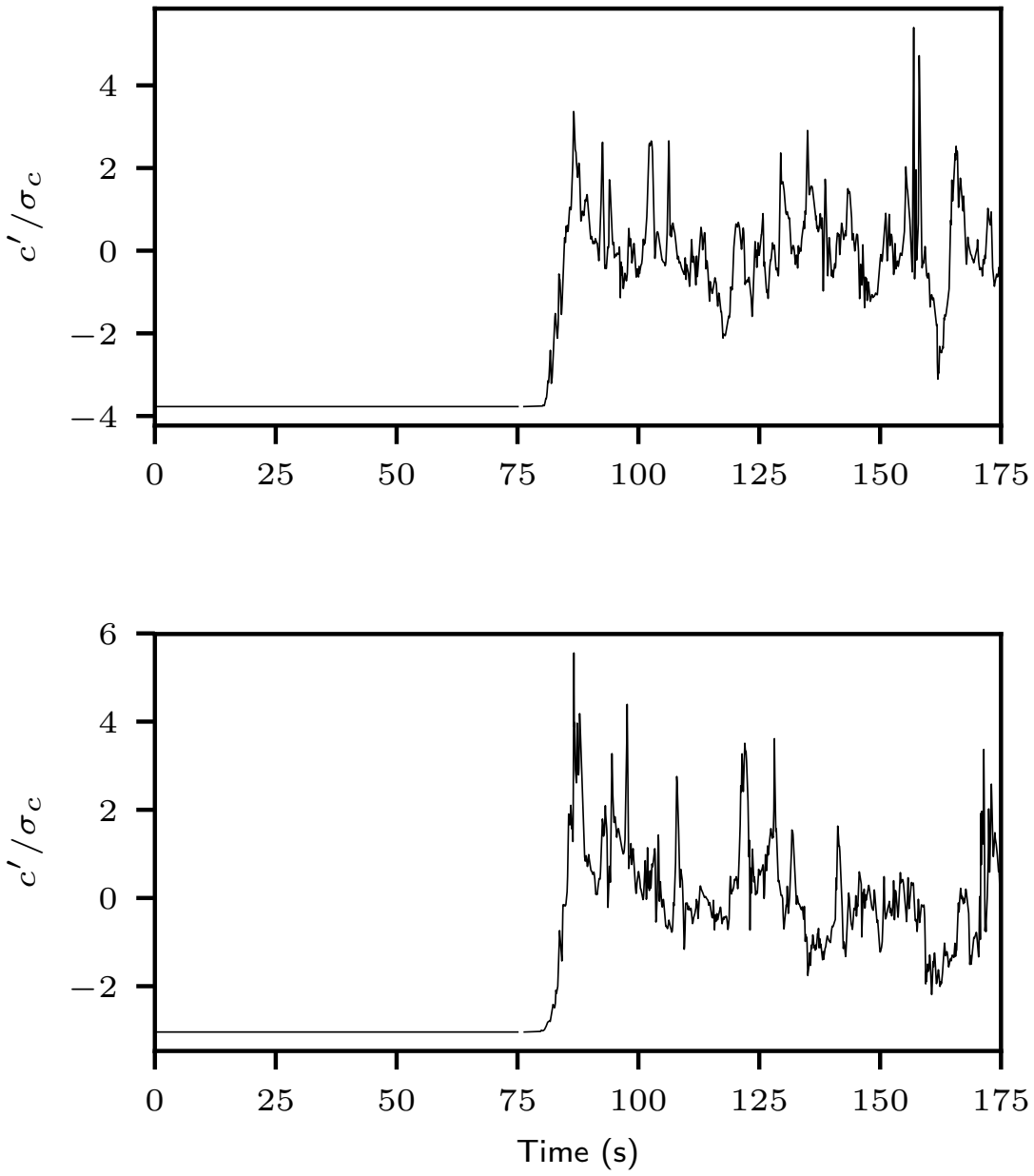

Figure 2.6: Example timeseries of instantaneous concentration from a two ensemble members. Normalized scalar concentration is shown on the y axis, and time is on the x axis. The sampled height is at 1.75 meters above the street $N_z = 9$ or $z/H = 0.175$. The concentration statistics are only taken from the sample period from 95 seconds to 175 seconds.

Chapter 3

Results

3.1 Flow Characteristics

Before an in-depth analysis of the plume moments and exposure is given, a brief diagnosis of the idealized UBL flow was performed comparing the two geometries. This will provide a framework for the plume discussion moving forward, and will help visualize the simulations more cohesively.

Time-averaged velocity fields were created to help pin-point differences in the flow for the two geometries. Figure 3.1 shows contour plots of this at $z/H \approx 0.5$. For the streamwise velocities, positive values of u indicate the fluid is traveling from left to right as shown in the diagram. Channeling along aligned streets is immediately apparent, with very high velocities along these street canyons. The staggered geometry is a significant barrier to the turbulent flow at street level, resulting in lower velocities throughout the domain at this height. There are also near zero or slightly negative velocities on the leeward side of the cuboids, indicative of eddies forming downwind of the obstacles. For the spanwise velocities $\bar{\tilde{v}}$, positive values indicate movement toward the top of the domain in this view. These velocities are notably larger in the staggered geometry (panel e), evidence of more significant lateral movement of the fluid. The vertical velocity field features eddies forming downwind of the cuboids, but they are noticeably stronger in the staggered cuboid case. The street configuration has average downward motion along the street at this height, with average upward motion in between cuboids, leading to very different shapes of the mean eddies between the two geometries.

Horizontal averaging of streamwise velocity field will help to generalize the differences within the geometries. Temporal averaging followed by spatial averaging is often called *double averaging* (DA) in urban meteorology literature (Kaimal and Finnigan 1994;

Finnigan 2000), so that terminology will be employed here. Figure 3.2 shows the results of DA on the normalized velocity profile. The aligned geometry features higher streamwise velocities below the top of the canopy, further evidence of momentum channeling. Around the max shear region $z/H = 1$, velocities are quite similar between the two geometries, but the aligned geometry shows higher velocities above the cuboids as well. The significant momentum fluxes induced by the staggered cuboids could translate into more substantial vertical mixing, resulting in lower momentum fluid being transported higher into the domain and a smaller magnitude velocity profile. All the while, preferential channeling in the aligned geometry may keep this lower momentum fluid within the canopy layer, and a larger magnitude velocity profile is the result.

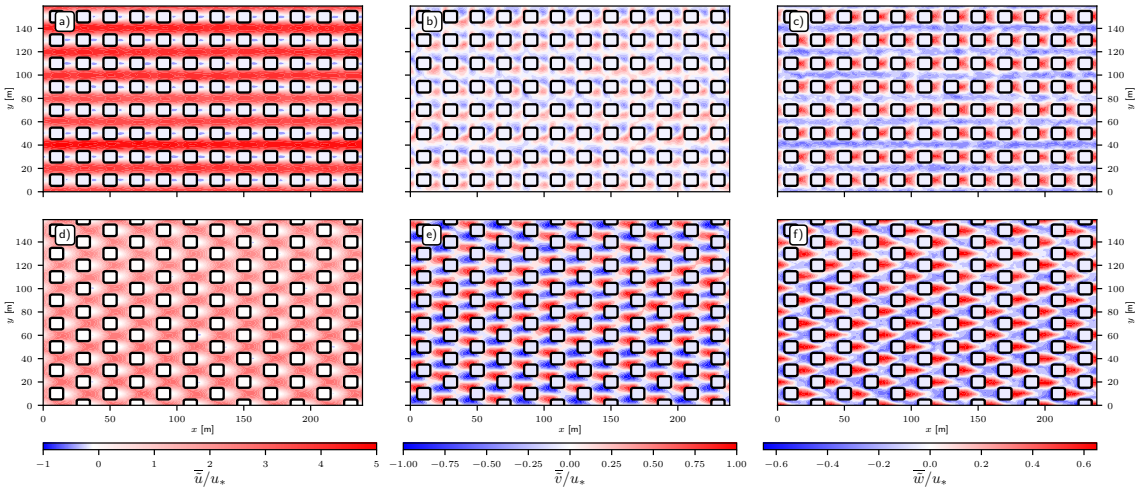

Figure 3.1: 2D cross-sections of time-averaged normalized velocities for the two idealized urban geometries at constant height. Each cross section is at $z/H = 0.5$. The top panels are for the aligned geometry, and the bottom panels are for the staggered geometry. Panels a) and d) show time-averaged streamwise velocity, panels b) and e) show time-averaged spanwise velocity, and panels c) and f) show time-averaged vertical velocity. All velocities are normalized by the friction velocity u^*.

More in-depth momentum statistics may diagnose more difference between the geometries. A similar analysis to the grid convergence tests was done here; horizontally averaged

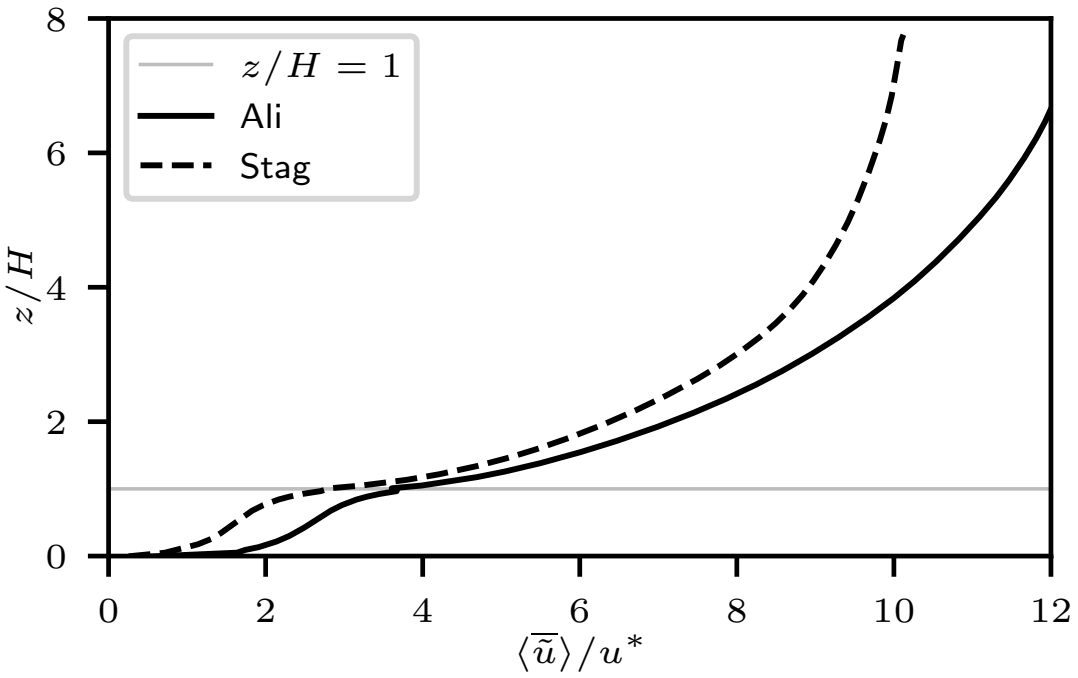

Figure 3.2: Vertical profile of normalized, double averaged (DA) streamwise velocity. Normalized height is on the y axis, and the top of the cuboids is marked by $z/H = 1$.

momentum statistics are compared between the two geometries. The results of this are shown in Figure 3.3. There are some significant differences in flow statistics between the two geometries. The streamwise variance is much larger for the aligned geometry below $z/H = 1$, while marginally lower above the canopy. Panel a) in Figure 3.1 shows highly positive and negative velocities at street level within the aligned geometry, and could be reflected in the high variance seen here. Spanwise variance in b) is the opposite - the staggered geometry has larger variance at street level, with lower variance above the canopy. Less channeling and a more significant barrier to streamwise velocities within the urban canopy in the staggered geometry may help to amplify the spanwise variance. Vertical velocity variance is similar for both geometries below the canopy, but slightly larger for the aligned geometry above the max stress region. The combination of resolved and SGS stress is similar for both geometries, but TKE reveals a major difference: within the cuboid canopy, the aligned geometry has higher TKE. Larger magnitudes in velocity seen in Figure 3.1 are also reflected in this. Above the urban canopy though, quick convergence between both geometries is evident in the TKE.

3.2 Scalar Plume Structure

More general scalar concentration behavior was explored before generating the specific plume moments. Time-averaged concentration plots for each of the simulations were created to help diagnose these characteristics of the plumes. Figure 3.4 shows different 2D slices of the time averaged normalized concentration for each of the three simulations setups. Horizontal and vertical spread of the plume is clearly evident for all three setups, which the overlaid plume moments confirm. The staggered geometry features higher concentration contours at greater lateral distances from y_{src} in panel e), a sign of more significant plume spread. The aligned geometry with the source in the street has higher concentration contours farther downstream of x_{src} than either of the other simulations, which points toward scalar channeling down the street aligned with y_{src}.

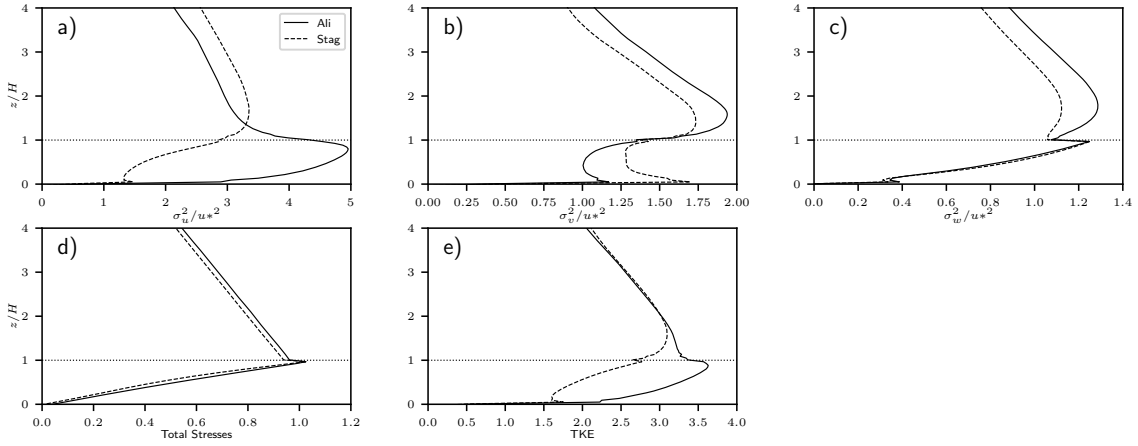

Figure 3.3: Comparison of momentum statistics between the aligned and staggered idealized canopies.Panels a), b), and c) show the horizontally averaged resolved velocity variance for the streamwise, spanwise, and vertical velocity components, respectively. These variances are all normalized by the friction velocity squared. Panel d) shows the combination of the resolved stresses and contribution from the SGS. Panel e) shows the horizontally averaged turbulent kinetic energy (TKE) of each flow. Vertical distance is normalized by building height H. The max shear region at $z/H = 1$ is marked for convenience.

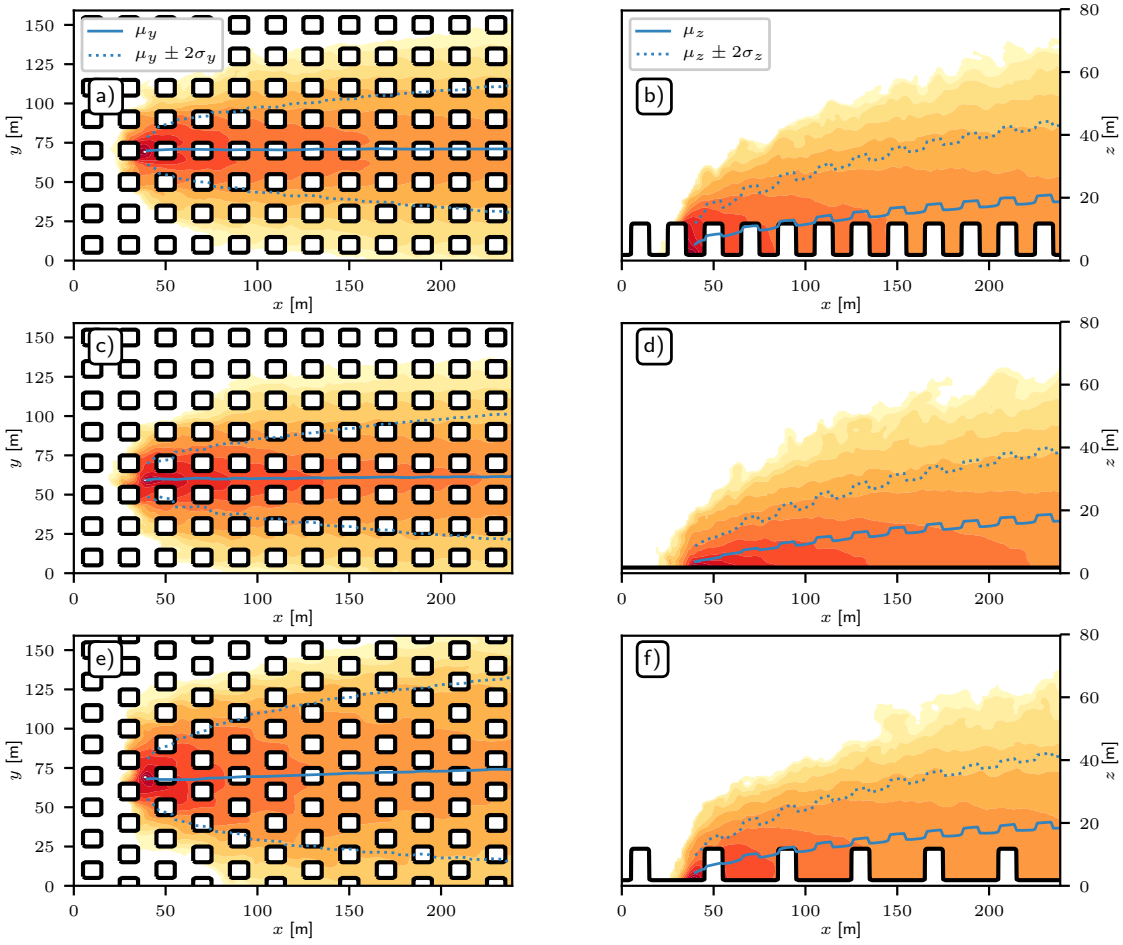

Figure 3.4: 2D cross-sections of time-averaged normalized concentration for the three idealized canopy setups. Contours are given in $\frac{\overline{\tilde{C}}u^*}{HQ_{src}}$ on a log scale from 10^{-8} to 10^{-2}. Panels a), c), and e) are XY cross-sections with z at z_{src} for the aligned, aligned in-street, and staggered canopy setups respectively. Panels b), d), and f) are XZ cross-sections with y at y_{src} for the aligned, aligned in-street, and staggered canopy setups respectively. The first and second plume moments are overlaid for each case.

Figure 3.5 shows a summary of the medium density simulation plume moments. For the horizontal plume centerline, deviation from the lateral source location is negligible with the largest deviation from source location at only ≈ 6 meters. It is unclear why the staggered geometry seems to favor this slight shift toward larger y valued centerlines. Source height is immediately apparent in the vertical centerlines, but has no distinguishing behavior other than different heights through the domain. The street source has a consistently lower plume centerline then either of the simulation setups, an effect of street channeling when the scalars are not immediately met with an obstacle downstream of the source. The lateral standard deviation features a much larger spread with all three of the staggered geometry simulations due to the amplified lateral momentum transfer. Note that $Stag_H$ has a slightly reduced spread compared to the lower two sources; with a source that high, many of the released scalars will simply pass over the cuboids. Near convergence with the aligned and street simulations is seen after about $15H$, meaning the plume becomes more or less independent of the geometry after this point. This emphasizes the importance of the near-source plume statistics when comparing geometries. The vertical standard deviations are closely aligned with one another.

For the higher order moments (skewness and kurtosis), the perfect Gaussian values are marked to easily distinguish non-Gaussian characteristics in the near source region. Horizontal skewness shows a convergence to near Gaussian ($sk = 0$) values after about $10H$, with a positive distribution closer to the source before this. Vertical skewness converges to values around 1 for all simulations after $10H$. This positive skewness is simply due to the higher concentration of scalars above the source height, and is not necessarily indicative of non-Gaussian characteristics when the lower boundary is that close to the source locations. Note that the high source heights seem to converge from negative Sk_z values near the source, while low source heights converge from even higher positive Sk_z values near the source. Lateral kurtosis shows very high values near the source, especially for the street simulations, before Gaussian convergence ($K = 3$) after about $12.5H$. Large kurtosis values

denote heavy center of distribution near the mean - this could be further evidence of street channeling. The same holds true for the vertical kurtosis - large positive values are clearly favored for the street simulations, and near Gaussian or slightly positive convergence is seen for all simulations after $15H$.

In addition to the moments, the maximum time-averaged concentration downstream of the source was calculated for each simulation, shown in Figure 3.6. Normalizing these values in an urban environment is non-trivial, so the raw maximum concentration from the grid cells is shown here. The street source configuration shows consistently higher maximum concentration values compared to the staggered and aligned setups. This could be a sign of significant channeling, as high concentration fluid directly downstream from the source will not interact with the buildings to the same degree as the other cases. Even in the near source region from $x/H = 2.5$ to 7.5, the street simulations, especially the low and mid source heights, show a dramatically higher maximum concentration. With the kurtosis and vertical centerline plots supporting this, the effects of street canyon channeling are a major result from these nine simulations.

While many moments showed clear dependence on source height, these findings are negligible compared to geometry and placement. Combine these results with our emphasis on human health and exposure, and we will keep our tower simulations focused on low sources near the fluid-solid interface to better simulate realistic pollutants dispersing at street level.

3.3 Exposure Statistics

Eight ensemble members were run within the medium density, aligned geometry, with the low source behind the cuboid. These ensembles, with about $12T_a$ per simulation, yields $\approx 96T_a$ of scalar sampling for each tower. Before exposure statistics are explored, statistical analysis of the raw instantaneous fields was performed. Joint (2D) PDFs of the instantaneous vertical and streamwise velocity components, along with the scalar concentration,

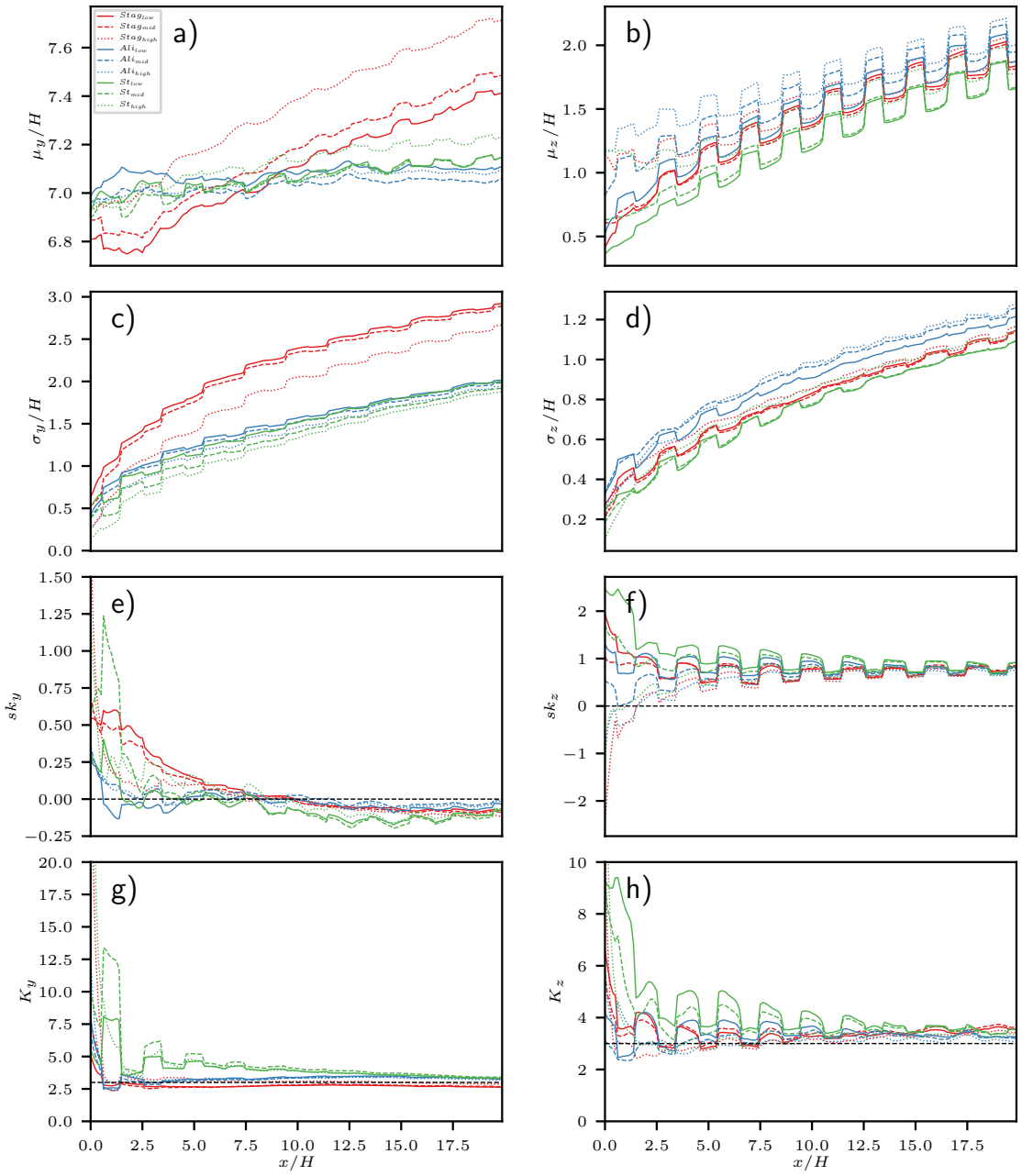

Figure 3.5: Plume moments for all nine of the simulations. Line type denotes source height, line color denotes geometry/placement. Each row represents a specific moment; Panels a) and b) refer to mean centerline, c) and d) the standard deviation (spread), e) and f) the skewness, and g) and h) the kurtosis. The columns denote the dimension of the moment; the left column refers to horizontal moments, and the right column refers to vertical moments. Downstream distances and moment values are normalized by the building height H.

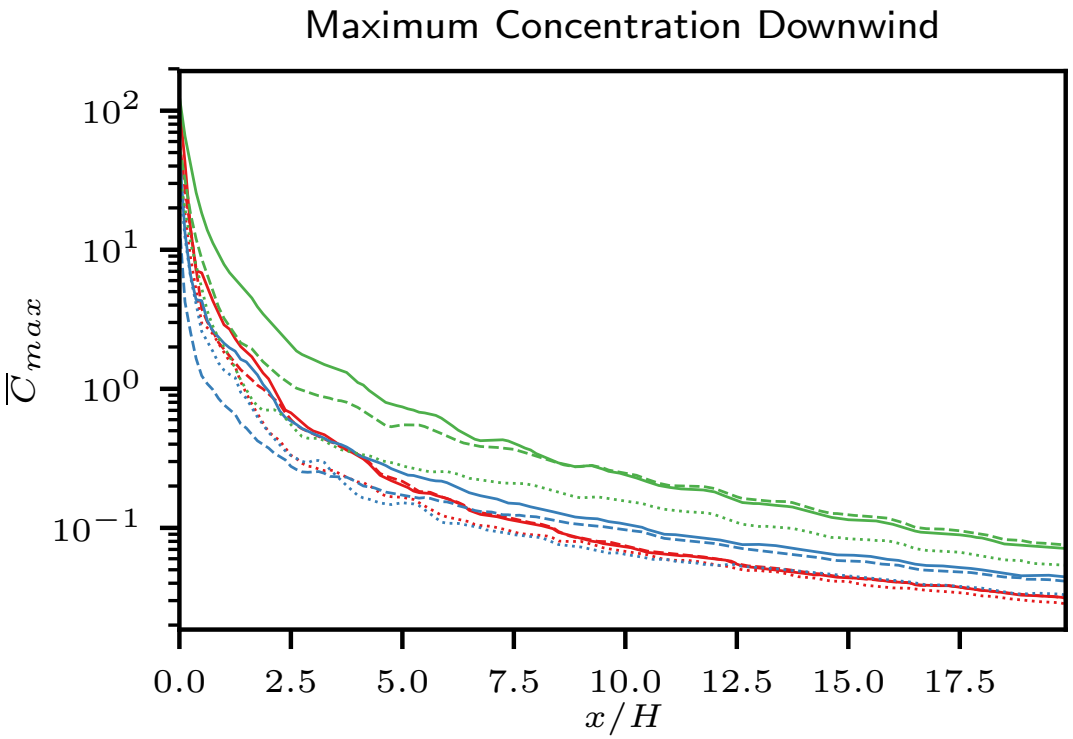

Figure 3.6: Maximum time-averaged concentration downstream from the source on a log-scale vs normalized distance from the source.

were created. Chamecki (2013) performed a similar analysis, but was not considering particle concentrations - only the velocity components. Figure 3.7 shows the results of this at building height for the tower along the centerline at $\mu_z = 1.5H$ (i.e., the center tower). Scalar concentration does not have significant correlation with either velocity component. Streamwise and vertical velocity distribution shows Quadrant II and IV preference, corresponding to ejections and sweeps respectively. This is typical in the max shear region around $z/H = 1$, and is supported by Chamecki (2013). JPDFs were also created for the same tower at street level (1.5 meters); these results are shown in Figure 3.8. There is equal weight in each quadrant for the momentum components in JPDF 3, a clear indication that there is no significant correlation between the streamwise and vertical velocity components below the max shear region at $z/H = 1$.

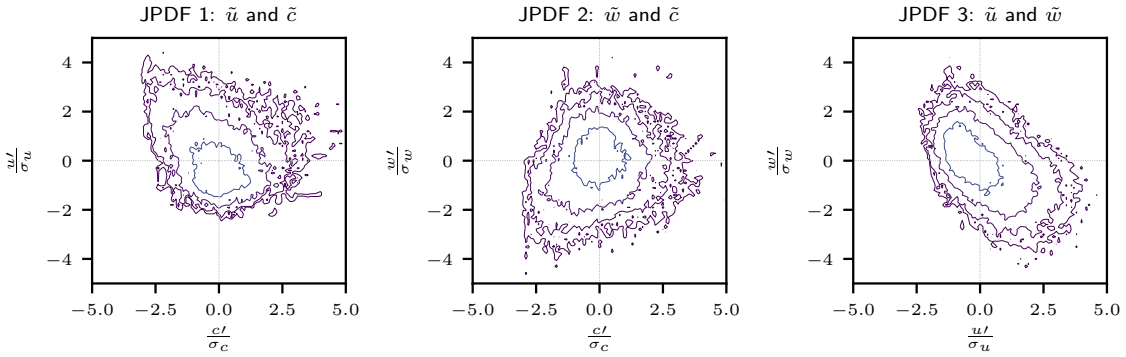

Figure 3.7: JPDFs for filtered instantaneous normalized streamwise and vertical velocity components, along with normalized scalar concentration values. Tower data is from the $\mu_z = 1.5H$ centerline tower at height $z/H \approx 1$. Contours are on a log scale from 0.001 to 0.4

A JPDF for the north tower at $z/H = 1$ was also created to deduce if the uncorrelated scalar concentrations are affected by domain placement. This is shown in Figure 3.9. A stark difference in JPDF behavior is noted here. While the momentum JPDF continues to show the preferential ejections and sweeps in Quadrants II and IV, the scalar concentration JPDFs show no values below $c'/\sigma_c \approx -1$. High correlations between the lower particle

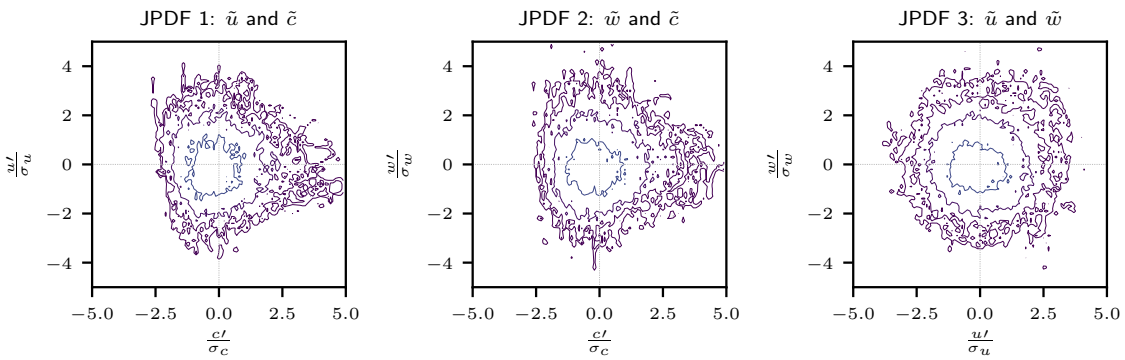

Figure 3.8: JPDFs for filtered instantaneous normalized streamwise and vertical velocity components, along with normalized scalar concentration values. Tower data is from the $\mu_z = 1.5H$ centerline tower at height $z/H = 0.15$. Contours are on a log scale from 0.001 to 0.4

concentrations and the mean velocities are seen on both of the scalar JPDFs. This suggests non-Gaussian behavior with the instantaneous scalar field — exposure statistics will help to characterise this behavior further.

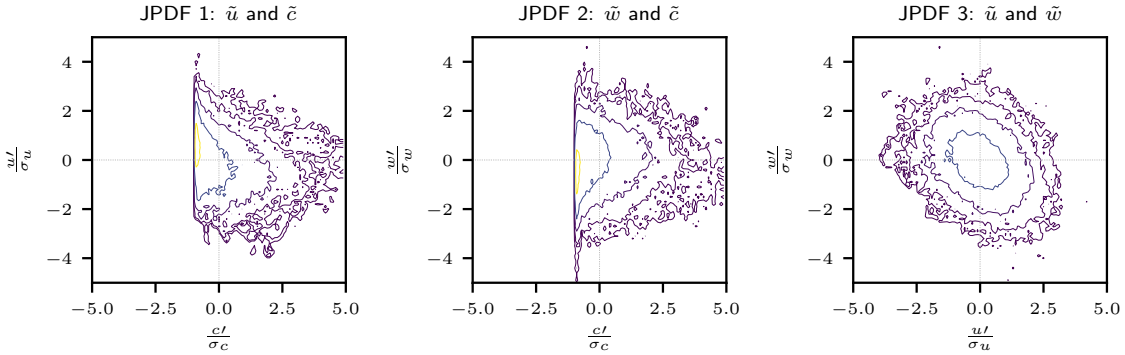

Figure 3.9: JPDFs for filtered instantaneous normalized streamwise and vertical velocity components, along with normalized scalar concentration values. Tower data is from the $\mu_z = 1.5H$, $2\sigma_y$ (north) tower at height $z/H = 1$. Contours are on a log scale from 0.001 to 0.4

For the exposure statistics, a positive $1\sigma_c$ threshold is used for the exceedance level. Figure 3.10 shows a comparison of probability density functions for each of the six towers under these conditions at the same height. The towers along the centerline, denoted by the solid lines, have higher exposure times for medium length events around 1 - 2 seconds, while fewer short events under one second. This suggests that exposure above $1\sigma_c$ tends to be more long-lasting for locations near the same lateral location as the source. It should be noted that the PDF tail for the towers not on the centerline is still substantial, suggesting that long-lasting exposure is prevalent on the plume edges even with preferential channeling.

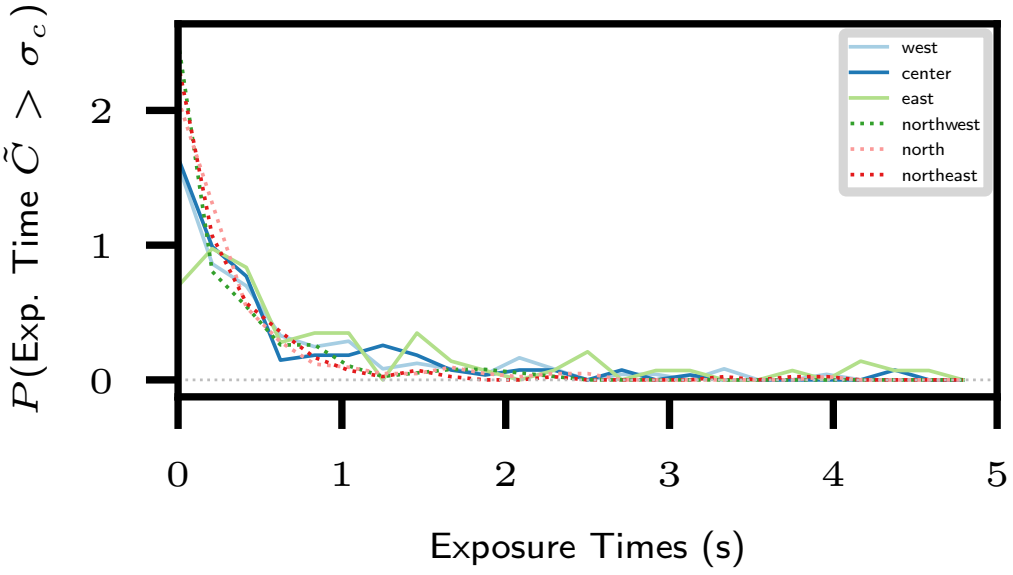

Figure 3.10: Probability density functions for each of the six towers in the medium, aligned, source-behind-street ensembles. Eight ensemble members are included here, and the height for each of the towers is 1.75 m above the bottom of the street canyon. Line type denotes centerline vs. $2\sigma_y$ towers. A $+1\sigma_c$ threshold is used.

To further characterise the scalar concentration at each tower, PDFs of raw and normalized concentration were created from the tower data as well. Figure 3.11 shows concentration PDFs for each tower location at the same height (street level). Two major modes of

behavior are immediately apparent. The raw concentration PDFs show a high probability of near zero concentration for the northern towers, with large positive tails on the north and northwest towers. The centerline towers have separate peaks in probability that appear to be a function of downstream location, with larger spread in concentrations on the center and western towers. On the normalized plot, all six towers feature quite large positive tails that extend beyond $+2.5\sigma_c$. The centerline towers roughly follow a Gaussian distribution to perhaps a Gamma distribution, with diminishing likelihood as concentrations lower. The northern towers show contrasting exponential PDFs, reflecting the high probability of near-zero concentration values seen in the raw PDFs. Despite the tendency for low mean concentration at the northern towers (i.e, near the plume edge), these data suggest significant exposure events are still possible well away from the plume centerline. Further, both of these plots indicate that assuming a Gaussian distribution is not appropriate to characterise instantaneous scalar concentration in certain regions of the plume - even where these exposure events are occurring.

To further visualize these findings, a collage of raw and normalized concentrations at each tower location from one ensemble member was created to spot any key differences in distribution. The results from this are shown in Figures 3.12 and 3.13. Intermittancy on the northern towers is clear in Fig. 3.12, with near-zero concentrations throughout much of the simulation interspaced with values comparable with concentrations at the centerline towers. Note the lower concentration values for the more downstream towers. The normalized collage features a quasi-Gaussian appearance for the centerline towers, all oscillating around the mean $c'/\sigma_c = 0$. An intermittent, non-Gaussian distribution is evident for the north towers. This results in large periods of time where concentration is near zero and $c'/\sigma_c < 0$, inter-spaced with large, $+2-3\sigma_c$ events. The high probability of slight negative c'/σ_c values in Figure 3.11 is also explained by this behavior, and further invalidates Gaussian assumptions about scalar exposure in certain regions of the domain. These intermittent

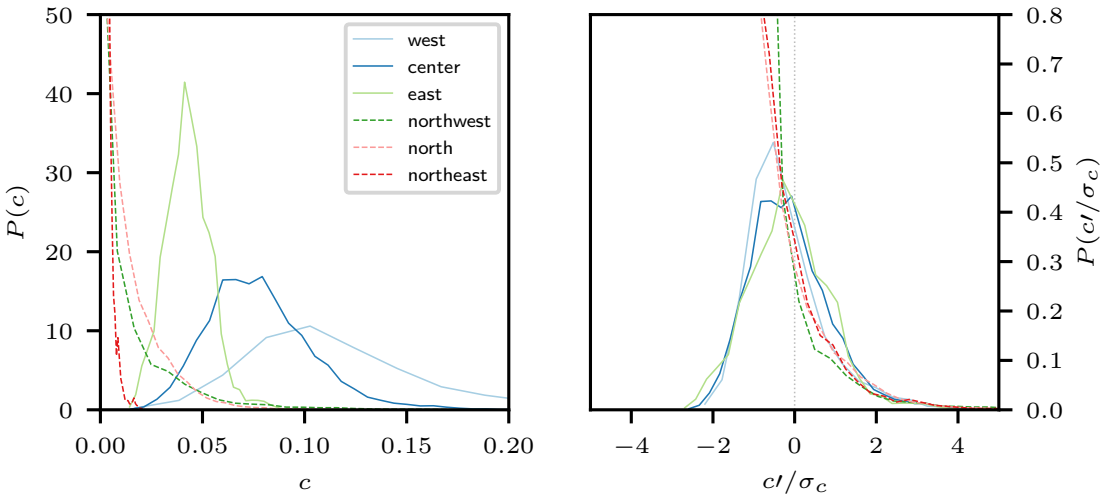

Figure 3.11: PDFs of raw (left) and normalized (right) concentration at each of the six tower locations. Height is 1.75 meters above the bottom of the street canyons. Dashed lines denote the northern $(+2\sigma_y)$ towers. The mean line is marked by a dashed grey line at $c'/\sigma_c = 0$ on the normalized plot.

concentrations were also found by Klein and Young (2011) near the plume edge, providing validation for the LES findings here with field data.

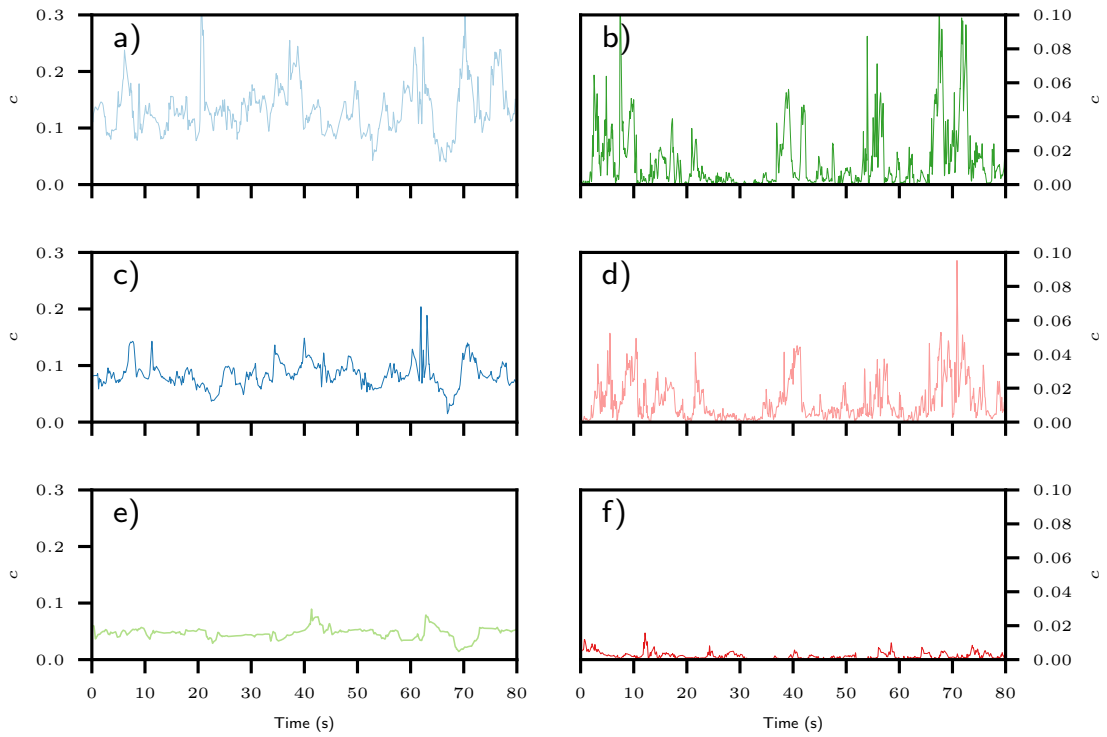

Figure 3.12: Collage of tower concentrations at the same height from one ensemble member. Panels a), c), and e) are for towers along the spanwise plume centerline (west, center, and east towers, respectively). Panels b), d), and f) are for towers along the $+2\sigma_y$ plume moment (northwest, north, and northeast, respectively). Concentration is on the y axis for each plot, with the entire tower sample period on the x axis. Separate y scales on the centerline and north towers are given for the sake of showing the contrasting behavior more effectively.

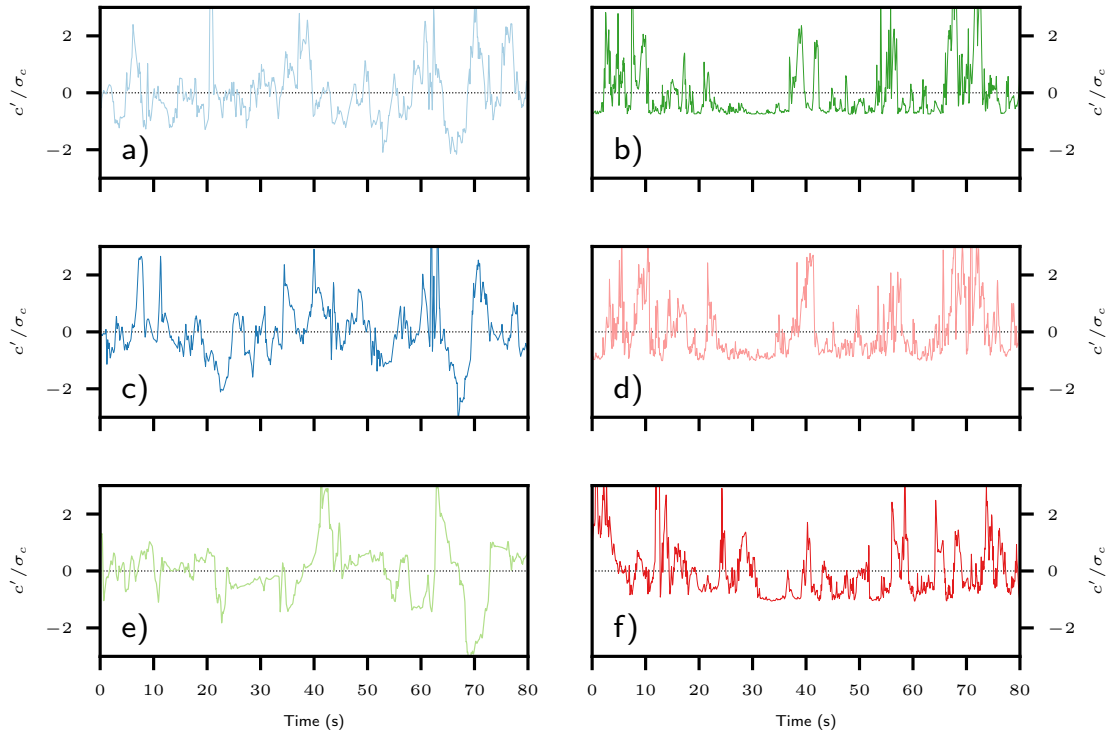

Figure 3.13: Collage of normalized tower concentrations at the same height from one ensemble member. Panels a), c), and e) are for towers along the spanwise plume centerline (west, center, and east towers, respectively). Panels b), d), and f) are for towers along the $+2\sigma_y$ plume moment (northwest, north, and northeast, respectively). Normalized concentration is on the y axis for each plot, with the entire tower sample period on the x axis. The mean concentration for each individual ensemble is marked by a dotted black line.

Chapter 4

Conclusions

Large eddy simulations with scalar transport have shown promising results in diagnosing plume and exposure behavior in an idealized urban canopy. The results from the simulations shown here help to diagnose this behavior in a number of ways. Source height was shown to affect scalar plume moments in a somewhat predictable fashion; mean centerlines and plume spread simply reflect their different starting heights and has little impact on their behavior otherwise. Urban geometry/configuration has a much more tangible effect on the plume moments. The staggered cuboids allowed for greater lateral spread in the plume, reflected by the large σ_y values when compared to the street or aligned setup. Kurtosis values were very large for the street source simulations in both y and z, indicative of abundant scalars immediately adjacent to the centerline. This suggests effective street channeling for the scalars leading to a distinctly non-Gaussian distribution. Plumes converged toward Gaussian values after $x/H \approx 12$, evidence that, regardless of urban geometry, the near-source region is characterised by these non-Gaussian features, and the far-region ($x/H > 12$) by Gaussian convergence. Widely used Gaussian-assumed dispersion models may work well far from the source, but fail to capture these non-Gaussian characteristics near the source. These results underline the importance of near-source urban dispersion field experiments and simulations to diagnose potentially hazardous plumes more accurately than current operational methods would. Higher-order plume moments Sk and K have not been explored in LES literature previously.

While plume moments are crucial towards diagnosing general plume shape and characteristics, they yield no information about local exposure within the plume, or the behavior of the instantaneous concentration field. The tower data from the LES provided a high temporal resolution data set to study this exposure, complete with spatial coverage when

multiple towers were added. Tower placement was dictated by the plume moments, resulting in a grid of towers downstream of the source location and encompassing various regions of the scalar plume. This instantaneous, domain-driven scalar analysis is the first of its kind in the LES literature. A wide variety of tower variables provided ample data to create JPDFs of scalar and momentum variables, and the streamwise and vertical velocity JPDFs showed the expected preference for sweeps and ejections in the max shear region. To diagnose exposure, arbitrary data-driven thresholds were used to determine exposure *times* above that threshold. While the exposure time PDFs suggested some relationship between plume location and local exposure, non-Gaussian instantaneous scalar behavior was clearly evident in the edges of the plume, where significant intermittency and exponential PDFs were found. In practice, this suggests that while mean concentration to some passive scalar or pollutant will be higher near the center of the plume, significant exposure events are very possible far from this plume centerline, perhaps more than what the plume moments would prescribe superficially. In the case of dangerous pollutants like PM2.5, human health implications arise from acknowledging the limitations of operational Gaussian dispersion models, and these results highlight the importance of doing so in the near source region and on the plume edges.

Future work in this area could focus on expanding the simulation space to other canopies, including more or less dense cuboids, variable cuboid heights, and tower simulations in other geometries. More tower coverage could yield a more complete picture of local concentration PDFs, and if enough are diagnosed, perhaps a predicative PDF model based on plume location could be explored. Heavy particles with intrinsic momentum (ie, not passive) could also be explored to account to deposition in an urban canopy.

Bibliography

Albertson, J. D., 1996: Large eddy simulation of land-atmosphere interaction. Ph.D. thesis, university of California, Davis, 1996.

Albertson, J. D., and M. B. Parlange, 1999: Surface length scales and shear stress: Implications for land-atmosphere interaction over complex terrain. *Water Resources Research*, **35 (7)**, 2121–2132, doi:10.1029/1999WR900094.

Belcher, S., O. Coceal, E. Goulart, A. Rudd, and A. Robins, 2015: Processes controlling atmospheric dispersion through city centres. *Journal of Fluid Mechanics*, **763**, 51–81, doi:10.1017/jfm.2014.661.

Belcher, S. E., 2005: Mixing and transport in urban areas. *Philosophical Transactions of the Royal Society A: Mathematical, Physical and Engineering Sciences*, **363 (1837)**, 2947–2968, doi:10.1098/rsta.2005.1673, URL https://royalsocietypublishing.org/doi/abs/10.1098/rsta.2005.1673, https://royalsocietypublishing.org/doi/pdf/10.1098/rsta.2005.1673.

Berkowicz, R., 2000: Ospm - a parameterised street pollution model. *Environmental Monitoring and Assessment*, **65 (1)**, 323–331, doi:10.1023/A:1006448321977, URL https://doi.org/10.1023/A:1006448321977.

Bornstein, R., 1987: Mean diurnal circulation and thermodynamic evolution of urban boundary layers. *Proceedings of Modeling the Urban Boundary Layer.*, **Boston MA, Am. Meteorol. Soc.**

Bosanquet, C. H., and J. L. Pearson, 1936: The spread of smoke and gases from chimneys. *Transactions of the Faraday Society*, **32**, 1249–1263.

Bou-Zeid, E., C. Meneveau, and M. Parlange, 2005: A scale-dependent lagrangian dynamic model for large eddy simulation of complex turbulent flows. *Physics of Fluids*, **17 (2)**, 025 105, doi:10.1063/1.1839152, URL https://doi.org/10.1063/1.1839152, https://doi.org/10.1063/1.1839152.

Bou-Zeid, E., J. Overney, B. D. Rogers, and M. B. Parlange, 2009: The effects of building representation and clustering in large-eddy simulations of flows in urban canopies. *Boundary-Layer Meteorology*, **132 (3)**, 415–436, doi:10.1007/s10546-009-9410-6, URL https://doi.org/10.1007/s10546-009-9410-6.

Briggs, G. A., 1973: Diffusion estimation for small emissions. preliminary report. *Technical Report*, doi:10.2172/5118833.

Britter, R. E., and S. R. Hanna, 2003: Flow and dispersion in urban areas. *Annual Review of Fluid Mechanics*, **35 (1)**, 469–496, doi:10.1146/annurev.fluid.35.101101.161147.

Chamecki, M., 2013: Persistence of velocity fluctuations in non-gaussian turbulence within and above plant canopies. *Phys. Fluids*, **25 (11)**, 115 110, doi:10.1063/1.4832955, URL https://doi.org/10.1063/1.4832955, https://doi.org/10.1063/1.4832955.

Chamecki, M., C. Meneveau, and M. B. Parlange, 2008: A hybrid spectral/finite-volume algorithm for large-eddy simulation of scalars in the atmospheric boundary layer. *Boundary-Layer Meteorology*, **128 (3)**, 473–484, doi:10.1007/s10546-008-9302-1.

Chan, T. L., and M. Lippmann, 1980: Experimental measurements and empirical modelling of the regional deposition of inhaled particles in humans. *American Industrial Hygiene Association Journal*, **41 (6)**, 399–409, doi:10.1080/15298668091424942, pMID: 7395753.

Chester, S., C. Meneveau, and M. B. Parlange, 2007: Modeling turbulent flow over fractal trees with renormalized numerical simulation. *Journal of Computational Physics*, **225 (1)**, 427 – 448, doi:https://doi.org/10.1016/j.jcp.2006.12.009.

Cionco, R. M., 1965: A mathematical model for air flow in a vegetative canopy. *Journal of Applied Meteorology*, **4 (4)**, 517–522, doi:10.1175/1520-0450(1965)004⟨0517:AMMFAF⟩2.0.CO;2.

Cramer, H. E., 1957: A practical method for estimating the dispersion of atmospheric contaminants. *Proc. 1st Natl. Conf. on Appl. Meteorol. Amer. Meteorol. Soc.*

Cui, Z., X. Cai, and C. J. Baker, 2004: Large-eddy simulation of turbulent flow in a street canyon. *Quarterly Journal of the Royal Meteorological Society*, **130 (599)**, 1373–1394, doi:10.1256/qj.02.150.

Davidson, M., K. Mylne, C. D. Jones, J. C. Phillips, R. J. Perkins, J. C. H. Fung, and J. C. R. Hunt, 1995: Plume dispersion through large groups of obstacles—a field investigation. *Atmospheric Environment*, **29**, 3245–3256.

Deardorff, J. W., 1972: Numerical Investigation of Neutral and Unstable Planetary Boundary Layers. *Journal of the Atmospheric Sciences*, **29 (1)**, 91–115, doi:10.1175/1520-0469(1972)029⟨0091:NIONAU⟩2.0.CO;2, URL https://doi.org/10.1175/1520-0469(1972)029⟨0091:NIONAU⟩2.0.CO;2, https://journals.ametsoc.org/jas/article-pdf/29/1/91/3417502/1520-0469(1972)029_0091_nionau_2_0_co_2.pdf.

EPA, 2018: Particulate matter (pm) pollution. Tech. rep., US Environmental Protection Agency.

Fernando, H. J. S., 2010: Fluid Dynamics of Urban Atmospheres in Complex Terrain. *Annual Review of Fluid Mechanics*, **42**, 365–389, doi:10.1146/annurev-fluid-121108-145459.

Finnigan, J., 2000: Turbulence in plant canopies. *Annual Review of Fluid Mechanics*, **32 (1)**, 519–571, doi:10.1146/annurev.fluid.32.1.519, URL https://doi.org/10.1146/annurev.fluid.32.1.519.

Gal-Chen, T., and R. C. J. Somerville, 1975: On the use of a coordinate transformation for the solution of the navier-stokes equations. *J. Comput. Phys.*, **17**, 209–228, doi:10.1016/0021-9991(75)90037-6.

Gaskell, P. H., and A. K. C. Lau, 1988: Curvature-compensated convective transport: Smart, a new boundedness- preserving transport algorithm. *International Journal for Numerical Methods in Fluids*, **8 (6)**, 617–641, doi:10.1002/fld.1650080602.

Germano, M., U. Piomelli, P. Moin, and W. H. Cabot, 1991: A dynamic subgrid-scale eddy viscosity model. *Phys Fluids A*, **3**, 1760–1765.

GHO, 2015: Urban health. Tech. rep., World Health Organization.

Gifford, F. A. J., 1961: Use of routine meteorological observations for estimating atmospheric dispersion. *Nuclear Safety*, **2**, 47–51.

Giometto, M., A. Christen, P. Egli, M. Schmid, R. Tooke, N. Coops, and M. Parlange, 2017: Effects of trees on mean wind, turbulence and momentum exchange within and above a real urban environment. *Advances in Water Resources*, **106**, 154 – 168, doi:https://doi.org/10.1016/j.advwatres.2017.06.018, tribute to Professor Garrison Sposito: An Exceptional Hydrologist and Geochemist.

Giometto, M. G., A. Christen, C. Meneveau, J. Fang, M. Krafczyk, and M. Parlange, 2016: Spatial characteristics of roughness sublayer mean flow and turbulence over a realistic urban surface. *Bound. Layer Meteorol.*, **160 (3)**, 425–452.

Griffiths, R., 1994: Errors in the use of the briggs parameterization for atmospheric dispersion coefficients. *Atmospheric Environment*, **28 (17)**, 2861 – 2865, doi:https://doi.org/10.1016/1352-2310(94)90086-8.

Hayati, A. N., R. Stoll, J. J. Kim, T. Harman, M. A. Nelson, M. J. Brown, and E. R. Pardyjak, 2017: Comprehensive evaluation of fast-response, reynolds-averaged navier–stokes, and large-eddy simulation methods against high-spatial-resolution wind-tunnel data in step-down street canyons. *Boundary-Layer Meteorology*, **164 (2)**, doi:10.1007/s10546-017-0245-2.

Janssen, N., P. Fischer, M. Marra, C. Ameling, and F. Cassee, 2013: Short-term effects of pm2.5, pm10 and pm2.5–10 on daily mortality in the netherlands. *Science of The Total Environment*, **463-464**, 20 – 26, doi:https://doi.org/10.1016/j.scitotenv.2013.05.062.

Kaimal, J., and J. Finnigan, 1994: *Atmospheric Boundary Layer Flows: Their Structure and Measurement*. Oxford University Press, URL https://books.google.com/books?id=ljbSonRztIcC.

Kanda, M., R. Moriwaki, and F. Kasamatsu, 2004: Large-eddy simulation of turbulent organized structures within and above explicitly resolved cube arrays. *Boundary-Layer Meteorology*, **112 (2)**, 343–368, doi:10.1023/B:BOUN.0000027909.40439.7c.

Klein, P., and D. T. Young, 2011: Concentration fluctuations in a downtown urban area. part i: analysis of joint urban 2003 full-scale fast-response measurements. *Environmental fluid mechanics*, **11 (1)**, 23–42.

Kolmogorov, A., 1941: The local structure of turbulence in incompressible viscous fluid for very large reynolds numbers (in russian). *Doklady Akademiia Nauk SSSR*, **30**, 301–305.

Kumar, V., J. Kleissl, C. Meneveau, and M. B. Parlange, 2006: Large-eddy simulation of a diurnal cycle of the atmospheric boundary layer: Atmospheric stability and scaling issues. *Water Resources Research*, **42 (6)**, doi:10.1029/2005WR004651.

Lilly, D. K., 1967: The representation of small-scale turbulence in numerical simulation experiments. *Proceedings of IBM Scientific Computing Symposium on Environmental Sciences Yorktown Heights, New York,*, **IBM form no. 320-1951,**, 195–209.

Lilly, D. K., 1992: A proposed modification of the germano subgrid-scale closure method. *Physics of Fluids A: Fluid Dynamics*, **4 (3)**, 633–635, doi:10.1063/1.858280.

MacDonald, R., R. Griffiths, and S. Cheah, 1997: Field experiments of dispersion through regular arrays of cubic structures. *Atmospheric Environment*, **31 (6)**, 783 – 795, doi: https://doi.org/10.1016/S1352-2310(96)00263-4.

Macdonald, R., R. Griffiths, and D. Hall, 1998: A comparison of results from scaled field and wind tunnel modelling of dispersion in arrays of obstacles. *Atmospheric Environment*, **32 (22)**, 3845 – 3862, doi:https://doi.org/10.1016/S1352-2310(98)80006-X.

Mahesh, K., G. Constantinescu, and P. Moin, 2004: A numerical method for large-eddy simulation in complex geometries. *Journal of Computational Physics*, **197 (1)**, 215–240, doi:10.1016/j.jcp.2003.11.031.

Meneveau, C., T. S. Lund, and W. H. Cabot, 1996: A lagrangian dynamic subgrid-scale model of turbulence. *Journal of Fluid Mechanics*, **319**, 353–385, doi:10.1017/S0022112096007379.

Mittal, R., and G. Iaccarino, 2005: Immersed boundary methods. *Annual Review of Fluid Mechanics*, **37 (1)**, 239–261, doi:10.1146/annurev.fluid.37.061903.175743.

Moeng, C. H., 1984: A large eddy simulation for the study of planetary boundary layer turbulence. *J. Atmos. Sci.*, **41**, 2052–2062.

Monin, A. S., and A. M. Obukhov, 1954: Basic laws of turbulent mixing in the atmosphere near the ground (in russian). *Trudy geofiz. inst. AN SSSR*, **24**, 163–187.

Ng, W.-Y., and C.-K. Chau, 2014: A modeling investigation of the impact of street and building configurations on personal air pollutant exposure in isolated deep urban canyons. *Science of The Total Environment*, **468-469**, 429 – 448, doi:https://doi.org/10.1016/j.scitotenv.2013.08.077.

Pardyjak, E. R., and R. Stoll, 2017: Improving measurement technology for the design of sustainable sustainable cities. *Measurement Science and Technology*, **28**.

Pasquill, F., 1961: The estimation of the dispersion of windborne material. *Met. Mag.*, **90**, 33.

Philips, D. A., R. Rossi, and G. Iaccarino, 2013: Large-eddy simulation of passive scalar dispersion in an urban-like canopy. *Journal of Fluid Mechanics*, **723**, 404–428, doi: 10.1017/jfm.2013.135.

Pope, S. B., 2000: *Turbulent Flows*. Cambridge University Press, 771 pp.

Prandtl, L., 1904: über flüssigkeitsbewegung bei sehr kleiner reibung. *Verhandlungen des III. Internationalen Mathematiker Kongresses*, **2**, 484–491.

Salesky, S. T., M. G. Giometto, M. Chamecki, M. Lehning, and M. B. Parlange, 2019: The transport and deposition of heavy particles in complex terrain: insights from an eulerian model for large eddy simulation. *arXiv preprint arXiv:1903.03521*, 1903.03521.

Santos, J. M., N. C. Reis, I. P. Castro, E. V. Goulart, and Z. T. Xie, 2019: Using large-eddy simulation and wind-tunnel data to investigate peak-to-mean concentration ratios in an urban environment. *Boundary-Layer Meteorology*, **172 (3)**, 333–350, doi:10.1007/s10546-019-00448-1, URL https://doi.org/10.1007/s10546-019-00448-1.

Schraufnagel, D. E., 2020: The health effects of ultrafine particles. *Experimental & Molecular Medicine*, **52 (3)**, 311–317, doi:10.1038/s12276-020-0403-3, URL https://doi.org/10.1038/s12276-020-0403-3.

Seinfeld, J. H., and S. N. Pandis, 2006: *Atmospheric Chemistry and Physics: From Air Pollution to Climate Change*. 1232 pp.

Smagorinsky, J., 1963: General circulation experiments with the primitive equations. *Mon. Wea. Rev.*, **91**, 99–164.

Sreenivasan, K. R., A. Prabhu, and R. Narasimha, 1983: Zero-crossings in turbulent signals. *Journal of Fluid Mechanics*, **137**, 251–272, doi:10.1017/S0022112083002396.

Stockie, J., 2012: The mathematics of atmospheric dispersion modeling. *SIAM Review*, **53**, 349–372, doi:10.1137/10080991X.

Stull, R., 1988: *An Introduction to Boundary Layer Meteorology*. 666 pp.

Sutton, O. G., 1947a: The problem of diffusion in the lower atmosphere. *Quarterly Journal of the Royal Meteorological Society*, **73 (317-318)**, 257–281, doi:10.1002/qj.49707331704.

Sutton, O. G., 1947b: The theoretical distribution of airborne pollution from factory chimneys. *Quarterly Journal of the Royal Meteorological Society*, **73 (317-318)**, 426–436, doi:10.1002/qj.49707331715.

Sutton, O. G., and G. C. Simpson, 1932: A theory of eddy diffusion in the atmosphere. *Proceedings of the Royal Society of London*, **135**, 143–165.

Tseng, Y.-H., C. Meneveau, and M. B. Parlange, 2006: Modeling flow around bluff bodies and predicting urban dispersion using large eddy simulation. *Environmental Science & Technology*, **40 (8)**, 2653–2662, doi:10.1021/es051708m, URL https://doi.org/10.1021/es051708m, pMID: 16683605, https://doi.org/10.1021/es051708m.

UNDESA, 2018: 2018 revision of world urbanization prospects. Tech. rep., United Nations Department of Economic and Social Affiars.

Walton, A., and A. Cheng, 2002: Large-eddy simulation of pollution dispersion in an urban street canyon—part ii: idealised canyon simulation. *Atmospheric Environment*, **36 (22)**, 3615 – 3627, doi:https://doi.org/10.1016/S1352-2310(02)00260-1.

WHO, 2015: Ambient (outdoor) air pollution. Tech. rep., World Health Organization.

Xie, Z.-T., and I. P. Castro, 2008: Efficient generation of inflow conditions for large eddy simulation of street-scale flows. *Flow, Turbulence and Combustion*, **81 (3)**, 449–470, doi:10.1007/s10494-008-9151-5, URL https://doi.org/10.1007/s10494-008-9151-5.

Zhou, Y., and J. I. Levy, 2008: The impact of urban street canyons on population exposure to traffic-related primary pollutants. *Atmospheric Environment*, **42 (13)**, 3087 – 3098, doi:https://doi.org/10.1016/j.atmosenv.2007.12.037.